Evaluation of the treatment planning system decimal ElectronRT and custom-made bolus for FLASH-irradiation

Mizgin Coskun

Supervisors

Crister Ceberg, Elise Konradsson, Kristoffer Petersson, Lund

π

Utvärdering av *decimal ElectronRT* dosplaneringssystem för konform FLASH-strålbehandling med optimerad-tjockleks bolus

Strålbehandling ges vid behandling av tumörer för att eliminera tumörceller och bota cancer. 30% av all cancer botas med strålbehandling och 50% av alla cancerpatienter får minst en strålbehandling. Vid strålbehandling överförs hög energi till tumörceller så att bindningarna som håller ihop DNA-molekyler bryts och på så sätt orsakas skada. Dock uppstår skada inte endast i tumörceller utan även i frisk vävnad, även om frisk vävnad har bättre reperationsförmåga jämfört med tumörceller. Vid strålbehandling försöker man uppnå en så konform dos som möjligt för att minska skada i normalvävnad, vilket innebär att strålningen riktas mot tumören medan man försöker undvika känslig frisk vävnad. Dock är det omöjligt att helt undvika att stråla och skada frisk vävnad.

Så tidigt som 1959 upptäcktes fördelen med att leverera strålningen under en mycket kort tid – några få millisekunder, av Dewey and Boag. De observerade en högre överlevnad hos bakterier som blev bestrålade med hög doshastighet jämfört med bakterier som blev bestrålade med låg doshastighet. Dock, dröjde det 55 år innan denna effekt återigen blev aktuell. År 2014 refererades bestrålning med ultrahög doshastighet som FLASH-radioterapi och det rapporterades om att FLASH-radioterapi kan användas för behandling av lungtumörer med total respons och minskade biverkningar.

Den besparande effekten uppstår när strålningen ges under en mycket kort tid, delar av en sekund, och medför bättre skoning av normalvävnad. Strålbehandling med FLASH har hittills endast provats på en enda människa med goda resultat i form av milda biverkningar. Genom att implementera FLASH kliniskt önskas framtida strålbehandlingar ge mindre biverkan. Alternativt, spekuleras det om att högre stråldoser kan ges till patienter för att bota dem fullständigt då stråldosen som ges idag begränsas av biverkningar.

Vid strålbehandling används det ett dosplaneringssystem. I ett dosplaneringssystem kan dos till olika volymer såsom riskorgan och tumörer simuleras, samt kan en visualisering av dosfördelningen i patient fås och olika vinklar för strålleverasen kan väljas för att optimera dosfördelningen så mycket som möjligt. I vissa fall användes även ett bolus som placeras på patients hud, vilket är av vävnadsliknande material. Syftet med boluset är att höja dosen till ytan och att åstadkomma en jämn bestrålad volym i tumören. Tjockleken på boluset kan väljas för att styra hur djupt dosen når i vävnaden.

I detta arbete utvärderades dosplaneringssystemet *decimal Electron RT*, *eRT*, från *.decimal*. Dessutom, utvärderas ett bolus med optimerad tjocklek, dvs. ett bolus där tjockleken varierar över ytan så att konformiteten maximeras, på ett skall-fantom för att se om dosfördelningen kunde blir mer homogen och konform. Resultaten visade att dosfördelningen var förbättrad, dock krävs fler mätningar för att avgöra hur väl dosplaneringsystemet simulerar den verkliga levererade FLASH-dosen.

Abstract

Introduction: The novel external beam therapy technique using ultra-high dose rates known as *FLASH* has become known for its normal tissue sparing effect. Currently in Lund, veterinary clinical trials are carried out on canine patients using electrons with ultra-high dose rates. By implementing a treatment planning system for FLASH-irradiation, the dose distribution can be visualized and the gantry and the couch angle can be optimized. Moreover, an optimized thickness bolus can be added to the treatment plan for a more conformal and homogeneous dose distribution inside the patient.

The aim of this master thesis is to evaluate the accuracy of the *decimal ElectronRT*, *eRT*, treatment planning system by *.decimal* for the purpose of implementing the eRT treatment planning system in future FLASH-irradiation treatments. In addition, the goal is to employ a custom-made optimized thickness bolus to a treatment plan inside the treatment planning system to determine if the treatment can be made more conformal. The custom-made optimized thickness bolus is provided by the treatment planning system

Material & Methods: Firstly, percentage depth dose curves and dose profiles were measured in a solid water phantom for different field sizes and at a source-to-surface distance (SSD) = 70 cm. The data was used to create a model of the modified linear accelerator used for FLASH-irradiation in the treatment planning system. Then, the model of the modified linear accelerator was used to create treatment plans for a solid water and an Alderson phantom. An SSD of 70 cm could not be used to create treatment plans due to a current limitation of the system. Hence, only an SSD of 100 cm was used and the plans were evaluated by new phantom measurements. Lastly, an optimized thickness bolus was added to the Alderson phantom treatment plan. Then, a new measurement on the Alderson phantom was made using the custom-made bolus with optimized thickness. The measurement was compared to the calculated dose profile exported from the treatment planning system.

Results: The identical repeated measurements of the percentage depth dose at SSD = 70 cm had their highest deviation values around 3%, except the percentage depth dose curve for the field size d = 3 cm. The comparison of the phantom measurements at SSD = 100 cm and the exported data from the treatment planning system showed good agreement. Although some differences could be seen for large field sizes, the deviation values of the full-width at half-maximum (FWHM) were not higher than 3%. The bolus measurement verified that a peak in dose, previously seen in measurements with no bolus, was effectively removed. Despite some differences that could be seen visually between the measured inline beam dose profile in Alderson phantom and the exported beam dose profile from the treatment planning system, the deviation value of the FWHM was not higher than 2%.

Conclusion: The eRT treatment planning system was evaluated and phantom measurements were performed for comparison purposes. Although the results indicate good agreement, further measurements are needed to verify the accuracy of the eRT treatment planning system at SSD = 70 cm, as the model data are based on an SSD = 70 cm. The results using optimized thickness bolus seem promising although further measurements are needed.

Contents

Abbreviations

CTV - Clinincal Target Volume

GTV - Gross Tumor Volume

OAR - Organs At Risk

OD - Optical Density

PDD - Percentage Depth Dose

PTV - Planning Treatment Volume

ROI - Region of Interest

RT - Radiation Therapy

SSD - Source to Surface Distance

STD - Source to Tray Distance

TPS - Treatment Planning System

1 Introduction

The novel external beam therapy technique using ultra-high dose rates known as *FLASH* has become a popular research topic, due to its reduced normal tissue toxicity compared to conventional radiotherapy [1]. Studies done in mice, mini-pig, and cat patients have provided encouraging results for further investigations of FLASH-irradiation [1][2].

External radiation therapy is used to treat tumors and different types of beams can be used, such as photons, electrons, and protons. Typically, conventional radiotherapy treatments are fractionated and it can take up to months to complete a treatment [3]. On the other hand, treatment with FLASH-irradiation may allow for the treatment to be delivered in fewer or with a single fraction, thus it can be more convenient for the patient.

FLASH-radiotherapy (FLASH-RT) has not been implemented clinically and so far it has only been used to treat one human patient with promising results [4]. By implementing FLASH-RT in clinical use, the side effects of treatments can be potentially reduced or the tumor effect can be improved by increasing the dose prescription. Moreover, the treatment time will be shortened, which can lessen the strain on patients and medical resources.

Currently in Lund, treatments of canine cancer patients are carried out using electrons at ultra-high dose rates at a source-surface distance (SSD) of 70 cm. The investigation by Konradsson et al. resulted in partial response, complete response, or stable disease in 11 of 13 tumors. The treatments are performed without a treatment planning system and the beam is described by measurements of depth dose curves and dose profiles for different field sizes. The assurance of prescribed dose is made by film measurements before and during the treatments, where also a Farmer-type ion-chamber was utilized for monitoring purposes [5]. By implementing a treatment planning system for FLASH-irradiation, the dose distribution can be quantified, in 3D volumetric dose statistics, visualized and adjusted such that organs at risk can be considered and avoided as much as possible while treating a tumor. Also, the gantry and the couch angle can be optimized for every beam.

In this study, the electron treatment planning system *decimal ElectronRT*, *eRT*, by *.decimal*, was utilized which is based on the pencil-beam redefinition algorithm and has the option of adding an optimized thickness bolus to a treatment plan with the capability of performing the bolus optimization. The aim of this master thesis is to evaluate and verify the accuracy of the electron treatment planning system eRT for FLASH-irradiation. The purpose is to enable the use of the eRT-software to accurately plan treatments for future veterinary patients treated with FLASH-RT. Additionally, using a custom-made bolus, the goal is to reduce possible heterogeneous dose distributions and unwanted hot and cold spots in irradiated volumes. For this, percentage depth dose curves and dose profiles were measured in phantoms using a linear accelerator modified for FLASH-RT delivery. The results were compared with the dose distribution computed by the eRT treatment planning system. Furthermore, a custom-made bolus was evaluated on the Alderson phantom to increase dose homogeneity, reduce hot spots and to obtain a higher conformity.

3

2 Theory

2.1 The Enlarged Therapeutic Window with FLASH-irradiation

There is increasing research evidence indicating that ultra-high dose rate irradiation, also known as *FLASH-irradiation*, can be used to widen the therapeutic window by sparing normal tissue while preserving the tumor-effect [1][2][4][6]. A study done by Favaudon et al. investigated the reduction of radiation-induced toxicities while preserving the tumor response, i.e. the FLASH-effect, in mice. It was observed that mice who received 20 Gy FLASH-irradiation did not have any formation of lung fibrosis or macroscopic visible signs of cutaneous lesions. On the other hand, the mice who received 17 Gy CONV-irradiation (conventional dose-rate irradiation, ≤ 0.03 Gy/s) experienced severe cutaneous lesions in the region of irradiation. Also, cachexia, pulmonary edema, and inflammatory lesions were observed in mice exposed to FLASH-irradiation at doses higher than 23 Gy. It was concluded that FLASH-irradiation has less fibrogenic effects compared to CONV-irradiation. In this study, it was also observed that FLASH-irradiation is as efficient as CONV-irradiation when it comes to control of tumors [1].

The FLASH-effect was also confirmed on bigger mammalians such as mini-pigs and cats with cancer through a study by Vozenin et al. The skin of a mini pig was irradiated to obtain a resemblance of the human skin. The mini pig received doses between 22-34 Gy, with electrons at both conventional dose rates (≈ 5 Gy/min) and ultra-high dose rates (≈ 300 Gy/s) on different skin patches. The results showed that FLASH-RT reduces damage to normal skin tissue by comparing 34 Gy FLASH-irradiated pig skin (resulting in depilation) to 28 Gy CONV-irradiated pig skin (resulting in fibronecrosis). The irradiation of cat patients was planned by a dose-escalation, where the initial dose was set to 25 Gy. When no dose limiting toxicity was found after 4 weeks of post-irradiation of the first cat patient, the next cat could be irradiated with a higher dose. In total, six cats were irradiated, and the dose was escalated up to 41 Gy. Although provisional side-effects were seen such as depilation, erythema, pigmentation, dry and moist desquamation, none of them were considered dose limiting toxicity. Three months post-radiotherapy treatment all six cats had macroscopic complete response. However, two of the cats that were given 28 Gy and 31 Gy, respectively, had a recurrence at 6- and 21-months post-irradiation. The dose escalation used on cat patients indicated that higher dose levels can be used when needed for complete tumor control while also resulting in manageable side-effects. The study concluded that the obtained results suggest further investigations on the use of FLASH-RT on human-patients [2].

Another article by Bourhis et al. described the treatment of the first patient with FLASH-radiotherapy using an electron beam. The patient, a 75-year-old man, had multiresistent cutaneous lymphoma spread over the skin surface. Formerly, the patient had been treated using local skin radiotherapy with KV and MV X-rays and low energy electrons. Given the radiosensitivity of the lesions, they could mostly be eliminated by giving 2 Gy/ fraction in 10 fractions or 3.5 Gy/fraction in 6 fractions. Nonetheless, the prescribed dose was enough to trigger an acute skin reaction, for instance, an irradiated lesion of 3-4 cm could take up to 3-4 months to heal. This resulted in the hypothesis that FLASH-RT may be adequate for this patient in helping to spare the normal tissue while maintaining

the tumor-effect. The patient received 10 pulses with 1.5 Gy/pulse in a single fraction with a total treatment time of 90 ms. These parameters were considered sufficient to trigger a FLASH-effect. The initial effects of the treatment could be seen such as mild redness on the skin. Additionally, mild edema was spotted under the skin, encircling the tumour. No deterioration of the thickness of the epidermis was observed. Nonetheless, a decrease in tumor size was noticed 10 days post-irradiation and full tumor-response was achieved 36 days post-irradiation. The patient received a biological equivalent dose, BED, (for α/β=10) of 37.5 Gy, which were 24 Gy and 28.35 Gy in previously local skin RT [4]. Considering the mild skin reactions and the high BED_{10} delivered in this study, the FLASH technique seems encouraging for further explorations. The results may suggest prescription of higher doses or greater sparing effects in future radiotherapy treatments with ultra-high dose rates.

2.1.1 The Radiobiological Mechanisms Behind the FLASH-effect

Although FLASH-irradiation has a sparing effect on normal tissue, the underlying radiobiological mechanisms are still not fully understood. A review by Wilson et al. evaluates the radiobiological evidence behind the FLASH-effect and whether FLASH radiotherapy can be used clinically. One hypothesis aimed to explain the reduction of normal tissue toxicity is *oxygen depletion* that occurs at ultra-high dose rates. The depletion occurs when the dose rate is so high that there is no time for new oxygen to be replenished, hence a hypoxic surrounding is formed. Hypoxic tissues are known to be more radioresistent compared to non-hypoxic tissues, due to the oxygen "fixating" the damage caused by radiation. Additionally, the absence of oxygen contributes to less production of cytotoxic radicals. Thereby, when the normal tissue gets depleted of oxygen it becomes more radioresistent. Following the same reasoning, oxygen depletion should also occur in tumor cells making the hypoxic cells even more hypoxic or even anoxic. However, with FLASH-irradiation the tumor-effect is not reduced - indicating that oxygen depletion is not the whole explanation of the mechanism behind the FLASH-effect. One suggestion is that the higher amount of redox-active iron in tumors, compared to normal tissues, produces more radicals and the difference in oxygen metabolism between tumor and normal tissue are the reasons behind the preserved tumor effect with FLASH-irradiation [6].

2.2 Interaction of Electrons in Matter

An electron, travelling in a medium will lose energy or scatter. The energy loss is described by the *Stopping Power* and the scattering is described by the *Scattering Power*. The electrons undergo Coulomb interactions with nuclei or orbital electrons, which can be elastic or inelastic. In an interaction between an electron and an orbital electron ionization or excitation can occur. The energy-loss in such collision is described by the mass collision stopping power , $(S/\rho)_{col}$. Interactions between electrons and atomic nuclei cause production of *bremsstrahlung* (X-ray photons). This kind of interaction is described by the mass radiative stopping power, $(S/\rho)_{rad}$. The total mass energy stopping power is the sum of these two components and is a characterization of the kinetic energy loss per unit

length of an electron traveling in a medium. It can mathematically be expressed as

$$(S/\rho)_{\text{tot}} = \frac{1}{\rho}\frac{dE_K}{dx} \tag{1}$$

where ρ is the density of the matter the electron interacts within, E_K is the kinetic energy lost by the electron and x is the path length the electrons travel [7].

Similarly, the mass scattering power can be expressed mathematically as

$$\frac{T}{\rho} = \frac{1}{\rho}\frac{d\overline{\theta^2}}{dl} \tag{2}$$

where ρ is the density of the matter the electron scatters within, $\overline{\theta^2}$ is the mean square angle of scattering and the l is the length of the absorber [7].

The interactions of electrons in water results in dose deposition along the depth in a particular reproducible pattern due to Coulomb interactions described above. This can be seen in a percentage depth dose, PDD, curve, which describes the relative dose, typically normalized to the maximum dose, as a function of the depth in water, see Figure 1 [7]. The surface dose is approximately between 80-100% and it builds up to a depth called z_{max} which is the depth where the dose is maximum. Beyond the electron beam depth of dose maximum, the dose reduces and a tail is obtained due to bremsstrahlung, which is approximately a few percent of the maximum dose. The bremsstrahlung tail is caused by the interactions of electrons and other materials when the beam leaves the linear accelerator. These materials are, for instance, the scattering foils, the transmission ionization chamber, water, and air [8]. The interactions also result in the broadening of the energy spectrum of the electron beam [7].

The percentage depth dose depends on parameters such as field size and the energy of of the electron beam. A larger field size will result in an increased z_{max}, i.e. the depth for maximum dose will increase and the surface dose will decrease, due to scattered radiation [7].
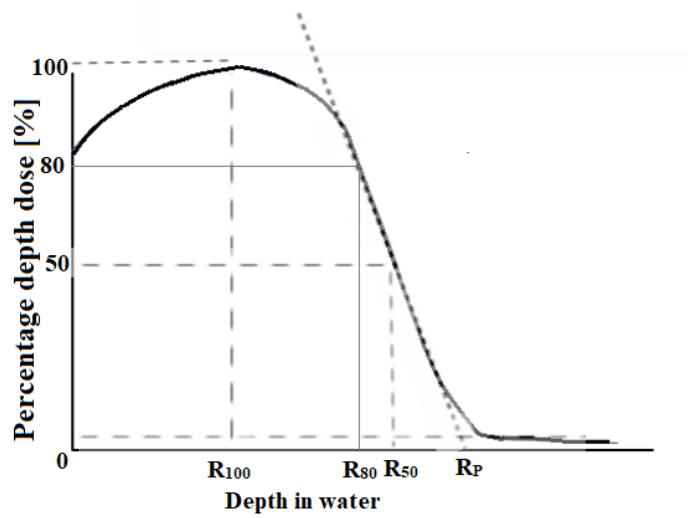
Figure 1: An illustration of a PDD curve for an electron beam. R_{100} is the depth of z_{max}, R_{80} and R_{50} are the depths where the dose is 80% and 50% of the maximum dose, respectively. R_P is the practical range and is defined at the intersection of the tangent through the steepest region in the curve and the the extrapolation line of the bremsstrahlung tail. It is considered that beyond the practical range only bremsstrahlung is deposited and no dose contribution from electrons is received [7]. The figure is a re-illustration from Podgorsak. [8].

The off-axis data of a beam can be obtained by measuring a profile in a phantom at typically z_{max} or 10 cm depth perpendicular to the beam central axis. The curve illustrates the relative dose as a function of the distance from the central axis of the beam, see Figure 2.
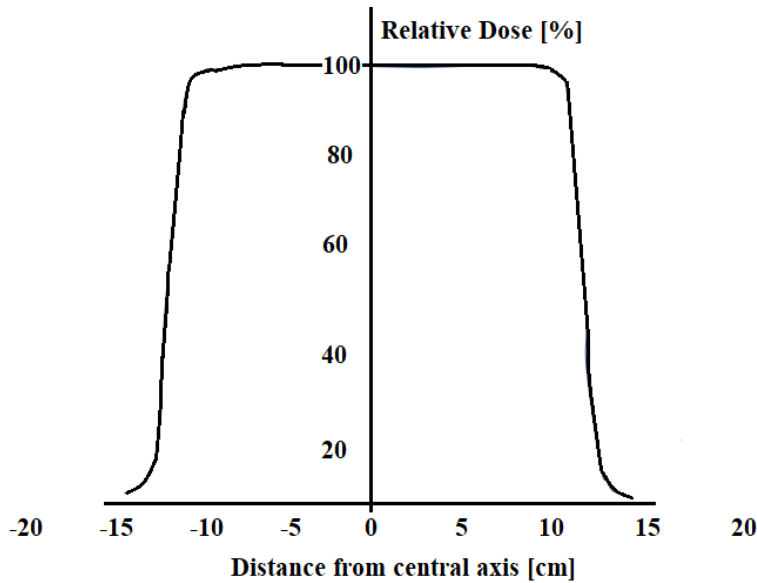
Figure 2: An example of a dose profile can be seen for an electron beam with an energy of 12 MeV and a 25x25 cm^2 applicator at a depth of dose maximum in water. The figure is a re-illustration from Podgorsak. [7].

To obtain a flat uniform beam at a certain depth, a dual foil scattering system may be used. Firstly, the electron beam is penetrated through a thin foil of high Z-material, which broadens the beam. This gives the beam a Gaussian-like shape. Next, the electron beam travels through a second foil with increased thickness of layers towards the center to obtain higher scattering in the center of the beam to flatten the dose profile [9].

To modify the electron beam size, applicators, also known as cones, are attached to the linear accelerator. The scattered radiation from these applicators affect the dose distribution inside the patient. This scattered radiation depends on the field size, the distance between the applicator and the patient surface, and the applicator design. Consequently, according to a study by Battum et al., the scattered radiation caused by the applicator in use should be incorporated into the treatment planning system [10].

2.3   Implementing FLASH in Clinical Setup

The initial step for implementing the FLASH technique into clinical use is to secure safe dose delivery. The prescribed dose needs to be delivered accurately to give patients adequate and safe treatment. In conventional radiotherapy, a calibrated built-in transmission ionization chamber is used for this purpose. It is used for monitoring and terminating the beam when the wanted dose of radiation has been delivered.

2.3.1 Modified Linear Accelerator to Obtain Ultra-high Dose Rates

To obtain a FLASH-effect, ultra-high dose rates (>30 Gy/s) are needed [11]. The ultra-high dose rates cannot be delivered by a conventional linear accelerator that normally delivers about 0.1 Gy/s. However, with a modification of the linear accelerator and the software, ultra-high dose rates can be obtained. This enables the use of a conventional linear accelerator for FLASH-irradiation with electron beams. For this, the primary and the scattering foils need to be removed so that the beam is not scattered, such that the desired dose rate can be achieved. Furthermore, the transmission chamber cannot be used to monitor and interrupt the beam when the wanted dose of radiation has been delivered. This is due to the ion recombination effects in the chamber in high dose per pulse beams as well as the relatively slow standard system for interrupting the beam delivery. Instead, an in-house built electrical circuit was used to manage the delivery of the electron beam on a pulse-by-pulse level. Several interlock software items needed to be deactivated because the linear accelerator was used outside of its normal clinical setting. To receive feedback about the delivered dose, a PIN diode was used as a detector, which counts the number of delivered pulses. The dose per pulse is measured by radiochromic film measurements. In this study, a linear accelerator (Elekta Precise from Elekta AB, Stockholm, Sweden) with integrated software version 1.2 was used, which were modified for ultra-high dose rates [11].

It is possible to use the built-in transmission chamber for beam monitoring purposes, however the reduced ion collection efficiency must be considered when the linear accelerator is used in FLASH-mode. A study done by Konradsson et al. investigated the chamber's drop in ion collection efficiency as a function of increased dose rate. By creating a model of the drop in ion collection efficiency with increased dose-per-pulse, the goal is to use the transmission chamber in a clinical setup with ultra-high dose rates to real-time monitor the beam delivery, although further testing is required [12].

2.3.2 Treatment Planning System in FLASH-radiotherapy

As mentioned in the introduction, the veterinary clinical trials are carried out without a treatment planning system (TPS). To implement a treatment planning system, the modified linear accelerator, used for FLASH-irradiation, needs to be incorporated into a software designed to generate treatments plans. Creating treatment plans using settings specified for a conventional linear accelerator would not work, due to the modified linear accelerator being changed, such as the dual foil scattering system being removed and a different applicator being used that normally is not used in conventional radiotherapy treatments. Hence, a treatment planning system commissioned for FLASH-RT is needed. Using a treatment planning system, the dose distribution in patients can be visualized and by outlining different structures, the dose to different volumes can be computed. Moreover, the gantry angle and the incidence angle can be optimized in every single beam. Currently in Lund, because there is no TPS commissioned for FLASH-RT, the treatment volume is estimated visually and with palpation and/or diagnostic CT-images.

Treatment planning systems are essential in radiation treatments since the dose distribution can be adjusted such that organ at risk (OAR) can be considered and avoided as

much as possible while treating a tumor [13]. Target volumes are outlined in diagnostic images. These volumes are gross tumor volume (GTV), which contains the magnitude of the tumor, the clinical target volume (CTV), which encircles the GTV and includes the expected microscopic part of the tumor, and planning treatment volume (PTV), which surrounds both GTV and CTV and includes a margin based on setup as well as uncertainties in the delivery and planning of the treatment [13].

After the outlining of GTV, CTV, PTV, and OAR using the software a plan for every beamline can be generated and the dose distribution inside the patient can be computed. What type of material the radiation will penetrate can be considered, such as muscle or bone, when computing the dose distribution inside the patient. In addition, plans can be created such that critical organs can be avoided or at least receive reduced dose. Moreover, a new plan or a modification of a plan can be made in case of a change in tumor size, making the treatment more conformal [14].

2.3.3 Pencil-beam Redefinition Algorithm

Algorithms are used in treatment planning systems to calculate the dose distribution in patients or phantoms [15]. One algorithm is the pencil-beam redefinition algorithm for electron dose distribution, derived by Shiu et al.

A pencil-beam is obtained by integrating a dose-spread function along an infinite ray of the incoming beam, starting from the surface and penetrating deeper in a volume. A dose-spread function characterizes the distribution of the absorbed energy from the secondary particles. Using a pencil-beam algorithm, the calculation speed can be increased compared to using the dose-spread function [16]. However the pencil-beam algorithm has limitations in terms of discontinuities in depth and laterally, when utilized on inhomogeneous volumes. On the other hand, the redefinition algorithm is based on redefining the parameters of an electron pencil beam continuously along the depth in tissue. The aim is to eliminate limitations related to such inhomogeneities. This is done by segregating the pencil beam into multiple components for different electron energies [15].

Firstly, the radiation transport is considered. The broad beam through the XY-plane at a depth z in a patient is composed by a group of small pencil beams. Properly, the pencil beam is expressed by a complex angular distribution. However, a Gaussian distribution is used to approximate the position of an arbitrary positioned pencil beam inside a patient [15].
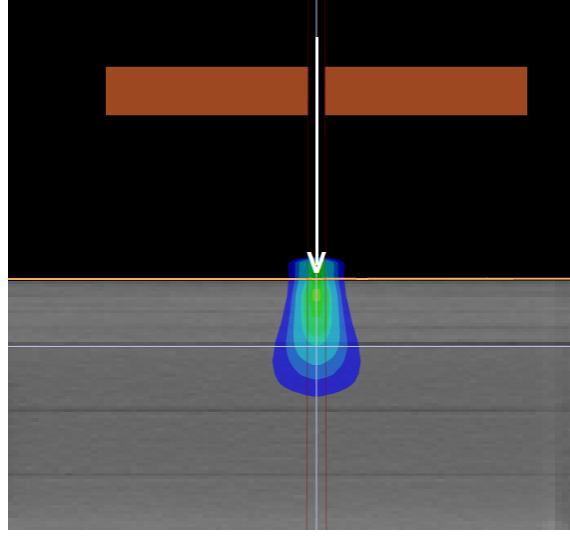
Figure 3: An electron dose distribution using pencil-beam redefinition algorithm is illustrated. The redefined pencil-beam kernel is obtained by integrating the scattered energy from the initial interaction, at the surface, along an infinite line while redefining parameters along the depth [17].

The electron dose distribution inside water, in the mth single energy bin can be expressed with the following equation

$$D_m^e(x_k, y_l, z + \Delta z) = \phi_m(x_k, y_l, z + \Delta z) \frac{S}{\rho}(\bar{E}_m) C(\bar{E}_m) \quad (3)$$

where $\phi_m(x_k, y_l, z + \Delta z)$ is the redefined fluence at $z + \Delta z$ for the mth energy bin. Δz is the tissue thickness. $\frac{S}{\rho}(\bar{E}_m)$ is the mass collision stopping power in water at the mean energy, $\bar{E}$, for the mth bin. $C(\bar{E}_m)$ is an experimentally determined correction factor at the mean energy for the mth bin. The correction factor is required due to only the most important physical interactions between electrons and tissue being modeled while the insignificant ones are ignored. The correction factor can be expressed simplified as

$$C^{WX,WY}(\bar{E}_z) \simeq \frac{\left[D_{H_2O}^{WX,WY;e}(0,0,z)\right]_{meas}}{\sum_{m=1}^{N_F} \phi_m(0,0,z) S/\rho(\bar{E}_m)} \quad (4)$$

where $\left[D_{H_2O}^{WX,WY;e}(0,0,z)\right]_{meas}$ is the electron dose component, obtained by

$$\left[D_{H_2O}^{WX,WY;e}(0,0,z)\right]_{meas} = \left[D_{H_2O}^{WX,WY}(0,0,z)\right]_{meas} - D_{H_2O}^{WX,WY_Y;\gamma}(0,0,z) \quad (5)$$

where $\left[D_{H_2O}^{WX,WY}(0,0,z)\right]_{meas}$ is the central axes depth dose measured in water and $D_{H_2O}^{WX,WY;\gamma}(0,0,z)$ is the photon dose component.

The fluence $\phi_m(x_k, y_l, z + \Delta z)$ can be calculated using following equation

$$\phi_m(x_k, y_l, z + \Delta z) = \sum_{i=1}^{N_x} \sum_{j=1}^{N_y} \frac{\Delta \phi_m^p(x_k, y_l, x_i, y_j, z + \Delta z)}{\cos \bar{\theta}_{i,j}^{k,l}} \quad (6)$$

11

where $\Delta\phi_m^p\left(x_k,y_l,x_i,y_j,z+\Delta z\right)$ is the increment of planar fluence for the mth bin and is calculated using following expression

$$\Delta\phi_m^p\left(x_k,y_l,x_i,y_j,z+\Delta z\right) = \sum_{n=1}^{N_E}\phi_n^p\left(x_i,y_j,z\right)\frac{1}{2}\left\{\mathrm{erf}\left[\frac{\theta_{x_k,\max}-\left(\bar{\theta}_{x_i}\right)_n}{\sqrt{2}\left(\sigma_{\theta_{x_iz+\varepsilon}}\right)_n}\right]-\mathrm{erf}\left[\frac{\theta_{x_k,\min}-\left(\bar{\theta}_{x_i}\right)_n}{\sqrt{2}\left(\sigma_{\theta_{x_iz+\varepsilon}}\right)_n}\right]\right\}$$

$$\times\frac{1}{2}\left\{\mathrm{erf}\left[\frac{\theta_{y_l\max}-\left(\bar{\theta}_{y_j}\right)_n}{\sqrt{2}\left(\sigma_{\theta_{y_jz+\varepsilon}}\right)}\right]-\mathrm{erf}\left[\frac{\theta_{y_l\min}-\left(\bar{\theta}_{y_j}\right)_n}{\sqrt{2}\left(\sigma_{\theta_{y_jz+\varepsilon}}\right)_n}\right]\right\}$$

(7)

where N_E is the number of energy bins and $\phi_n^p\left(x_i,y_j,z\right)$ is the planar fluence in the nth bin. ε is a thin layer where it is assumed that the tissue thickness is compressed within and where the interaction of electrons and tissue occur. θ_{x_k} and θ_{y_l} are the angles which the electrons scatter in after interacting with tissues, where they are scattered to a depth of $z+\Delta z$. $\sigma_{\theta_{x_iz+\varepsilon}}$ and $\sigma_{\theta_{y_jz+\varepsilon}}$ can be obtained using the following definitions

$$\left(\sigma_{\theta_{x,z+\varepsilon}}^2\right)_n\left(x',y',z+\varepsilon\right)\equiv\left(\sigma_{\theta_x'}^2\right)_n\left(x',y',z\right)+\frac{T_n\left(x',y',z\right)}{2}\Delta z \tag{8}$$

and

$$\left(\sigma_{\theta_{y,z+\varepsilon}}^2\right)_n\left(x',y',z+\varepsilon\right)\equiv\left(\sigma_{\theta_y'}^2\right)_n\left(x',y',z\right)+\frac{T_n\left(x',y',z\right)}{2}\Delta z \tag{9}$$

where $\left(\sigma_{\theta_x'}\right)_n$ and $\left(\sigma_{\theta_y'}\right)_n$ are the root-mean-square (rms) projected angular spread of electrons for the nth bin and $T_n\left(x',y',z\right)$ is the linear angular scattering power for electrons at the position $\left(x',y',z\right)$.

$\bar{\theta}_{x_i}$ and $\bar{\theta}{y_j}$ are the projected mean direction on XZ- and YZ-plane, respectively. At a position $\left(x_k,y_j,z+\Delta z\right)$ for the mth bin, the projected mean direction can be calculated as

$$\left[\bar{\theta}_x\left(x_k,y_l,z+\Delta z\right)\right]_m = \sum_{\substack{n=1\\ \ni E_m\leqslant\left(E_{ni,j}^{k,l}\right)_n<E_{m+1}}}^{N_E}\sum_{i=1}^{N_x}\sum_{j=1}^{N_y}\phi_n^p\left(x_i,y_j,z\right)$$

$$\times\left[\frac{\left(\sigma_{\theta_{x_iz+\varepsilon}}\right)_n}{\sqrt{2\pi}}\left(\exp\left\{\frac{-\left[\theta_{x_k,\min}-\left(\bar{\theta}_{x_i}\right)_n\right]^2}{\left(2\sigma_{\theta_{x_iz+\varepsilon}}^2\right)_n}\right\}-\exp\left\{\frac{-\left[\theta_{x_k,\max}-\left(\bar{\theta}_{x_i}\right)_n\right]^2}{\left(2\sigma_{\theta_{x_iz+\varepsilon}}^2\right)_n}\right\}\right)\right.$$

$$\left.+\frac{\bar{\theta}_{x_i}}{2}\left\{\mathrm{erf}\left[\frac{\theta_{x_k,\max}-\left(\bar{\theta}_{x_i}\right)_n}{\sqrt{2}\left(\sigma_{\theta_{x_iz+\varepsilon}}\right)_n}\right]-\mathrm{erf}\left[\frac{\theta_{x_k,\min}-\left(\bar{\theta}_{x_i}\right)_n}{\sqrt{2}\left(\sigma_{\theta_{x_iz+\varepsilon}}\right)_n}\right]\right\}\right]$$

$$\times\frac{1}{2}\left\{\mathrm{erf}\left[\frac{\theta_{y_l\max}-\left(\bar{\theta}_{y_j}\right)_n}{\sqrt{2}\left(\sigma_{\theta_{y_jz+\varepsilon}}\right)_n}\right]-\mathrm{erf}\left[\frac{\theta_{y_j\min}-\left(\bar{\theta}_{y_j}\right)_n}{\sqrt{2}\left(\sigma_{\theta_{y_jz+\varepsilon}}\right)_n}\right]\right\}/\phi_m^p\left(x_k,y_l,z+\Delta z\right)$$

(10)

Notice that Eq.(10) describes the projected mean direction on XZ-plane. Correspondingly, the projected mean direction on YZ-plane can be calculated using a corresponding expression.

To obtain the mean energy in Eq.(3) the following equation can be used

$$
\begin{aligned}
\bar{E}_m\left(x_k, y_l, z + \Delta z\right) = & \left(\sum_{\substack{n=1 \\ \ni E_m \leqslant \left(E_{ni,j}^{k,l}\right)_n < E_{m+1}}}^{N_E} \sum_{i=1}^{N_x} \sum_{j=1}^{N_y} \left(E_{i,j}^{k,l}\right)_n \phi_n^p\left(x_i, y_j, z\right) \right. \\
& \times \frac{1}{2} \left\{ \operatorname{erf}\left[\frac{\theta_{x_k,\max} - \left(\bar{\theta}_{x_i}\right)_n}{\sqrt{2}\left(\sigma_{\theta_{x_i z+\varepsilon}}\right)_n}\right] - \operatorname{erf}\left[\frac{\theta_{x_k,\min} - \left(\bar{\theta}_{x_i}\right)_n}{\sqrt{2}\left(\sigma_{\theta_{x_i,z+\varepsilon}}\right)_n}\right] \right\} \\
& \left. \times \frac{1}{2} \left\{ \operatorname{erf}\left[\frac{\theta_{y_l,\max} - \left(\bar{\theta}_{y_j}\right)_n}{\sqrt{2}\left(\sigma_{\theta_{y_j z+\varepsilon}}\right)_n}\right] - \operatorname{erf}\left[\frac{\theta_{y_l \min} - \left(\bar{\theta}_{y_j}\right)_n}{\sqrt{2}\left(\sigma_{\theta_{y_j z+\varepsilon}}\right)_n}\right] \right\} \right) \Big/ \phi_m^p\left(x_k, y_l, z + \Delta z\right)
\end{aligned}
\tag{11}
$$

where $E_{i,j}^{k,l}$ is the energy of electrons that fall into the nth bin. ϕ^p is the planar fluence in the mth and n^{th} bin respectively. $\sigma\theta_{x_i z+\varepsilon}$ and $\sigma_{\theta_{y_j z+\varepsilon}}$ can be obtained using Eq.(8) and Eq.(9) [15].

Additionally, a photon dose component needs to be considered, due to the production of bremsstrahlung [18]. It is considered that the dose contribution beyond the practical range of electrons is caused by the deposition of bremsstrahlung. Hence, by making an inverse square correction the photon dose component can be obtained [18].

Finally, the total dose is obtained by summing the electron dose component and the photon dose component

$$
D(x,y,z) = [D^e(x,y,z)] + [D^\gamma(x,y,z)]
\tag{12}
$$

Furthermore, the pecil beam redefinition calculated dose distribution was compared to measured dose distributions for homogeneous water phantom and for inhomogeneous depth-to-surface phantoms by Shiu et al. [15]. The results were in accordance, with a certainty within 4%. In regions such as the edges of air and bone inhomogeneities and the penumbral region resulted in better agreement between calculations and measurements compared to previously used pencil beam algorithms [15].

2.3.4 Radiochromic Film-based Dosimetry

A complementary method is required for obtaining the dose distribution in a patient or a phantom in cases where a TPS is not calibrated for absolute dosimetry or a quality assurance of a TPS needs to be done. One alternative is radiochromic film-based dosimetry .

When a radiochromic film is exposed to radiation, a color change can be observed on the macroscopic level [19]. The effect occurs due to the polymerization on microscopic level, i.e. the energy of a particle or a photon is transferred to a photo monomer molecule. In this process, visible light is attenuated resulting in the darkening of the film. This color change can be associated with the absorbed dose in the film. As more light is attenuated

the film gets darker, which is measured by the *optical density, OD*. The relation for optical density is the following

$$OD = log_{10}\left(\frac{I_0}{I}\right) \tag{13}$$

where I_0 is the intensity of unexposed film and I is intensity of the exposed film. The relation between the dose and I_0/I is exponential - making the relationship between the dose and the optical density linear until saturation is reached [20].

Generally, the dose measurements are done relatively, which reduce any risk of systematic errors [20]. The percentage depth dose and beam dose profiles of different ionizing beams can be measured using radiochromic films [19]. The optical density of the film can be expressed as the sensitivity of the film to the dose. This sensitivity depends on the photon beam energy, film plane orientation and the tools for analyzing. Hence, the films are usually calibrated for specific parameters [20]. Typically, the radiochromic film consists of one or two active layers of radiation sensitive material which can be a sort of crystalline polyacetylenes called dyacetilenes [19]. The thickness of the active layer can differ from batch to batch. Radiochromic film does not need any chemical or physical post-irradiation processing. However, the process of polymerization continues after the irradiation of the film is finished. The stabilization usually occurs between 24-48h post-irradiation, this results in a delay time between the irradiation and the scanning of the film. While the radiochromic film is not very sensitive to room light, it is sensitive to radiation from several types of particles, such as photons, electrons, and protons [20]. Another advantage of using radiochromic film is its independence of the dose rate. A study by Jaccard et al. investigated the suitability of Gafchromic EBT3 films for reference dosimetry for high dose-per-pulse electron beams with a mean dose rate between 0.07 - 3000 Gy/s and a dose rate in pulse up to $8 \cdot 10^6$ Gy/s. To investigate the mean dose rate, Gafchromic films were irradiated using four different dose rates: 0.55, 1.10, 2.20, and 4.40 Gy/min by delivering 100, 500 and 1000 MU. The results showed no dependency of the mean dose rate with the uncertainties taken into account. To investigate the dose rate in a pulse, two methods were used. First, the correlation between the dose rate in a pulse and the charge per pulse (obtained by a beam monitoring system) was investigated. Next, the dose rate in a pulse was studied by comparison of film and TLD doses between 2 to 20 Gy, for dose rates between $7 \cdot 10^3$ - $8 \cdot 10^6$ Gy/s. The results of the correlation showed a proportionality between the dose in a pulse and the dose rate in a pulse, hence indicating a dose rate independence of the Gafchromic EBT3 films. The comparison of Gafchromic EBT3 films and TLD showed that the films are not dependent on the dose rate over the investigated dose range [19].

EBT3 Gafchromic film is a type of radiochromic film that can be used in film dosimetry. A study done by Sorriaux et al. evaluated the uncertainties and characteristics of EBT3 Gafchromic films used in radiochromic film-based dosimetry [21]. The tested parameters were the reproducibility, inter- and intra-uniformity, orientation of the film and reading delay after irradiation and the effect of background light. This was done for several absorbed doses - 0.4 Gy, 2 Gy and 6.5 Gy. The parameters were tested by measuring the intensity of the exposed films, I_{exp}, intensity of unexposed films, I_{unexp} and intensity of zero light transmission, I_{bckg}. The results showed that the reading reproducibility could be

verified within a standard deviation 0.01%, of I_{exp}. The local film uniformity showed an increase with increased dose. The films were seen to get darker up to 46h post-irradiation and were stabilized after 48h post-irradiation with an uncertainty <0.01% of the I_{exp}. The effect of background light was concluded to be minimal. The uncertainties of I_{exp} related to orientation and scanner uniformity could be kept below 0.1% by always using the same position and orientation during film scanning. Despite the drawbacks of using films, such as the delay time between radiation and scanning and the need of a calibration curve for every single beam energy, the total uncertainty on the calibration curve for electrons of 2% for doses over 0.8 Gy makes EBT3 Gafchromic films reliable for uses in dosimetry [21].

2.3.5 Conformal Treatment Using Custom-made Bolus

Custom made bolus can be used to achieve a conformal electron treatment. This will prevent any cold or hot spots or unnecessary radiation to normal tissue.

To generate the electron bolus design, algorithms are used. A study by Low et al. explains the bolus design algorithms. Firstly, it is explained that there are no unique solutions for the design of bolus due to electron multiple scatter. Nonetheless, by creating three categories of operators, which are *creation*, *modification*, and *extension* operators, sufficient delivery of dose to the target, avoidance of organs at risk and homogeneous dose distribution within irradiated volume can be obtained [22].

The creation operators give the initial thickness of the bolus, by limiting the bolus thickness sum and the depth of PTV to the therapeutic range, R_t, along every fan line that is within the bolus margin inside the PTV . The bolus margin emanates from the target volumes usually having edges that can result in high dose gradients, hence the area of the bolus design is reduced by a bolus margin, Δ. The operator, $\mathbf{P}$, can be expressed as

$$\mathbf{P} = \mathbf{P}\left(\Delta, R_t\right) \tag{14}$$

The bolus thickness is only modeled along rays within the bolus margin inside the target , this region is referred to as target volume less margin (TVLM). This is due to large scatter at the lateral boundaries into the center of the radiation field due to the surface near the boundaries being smaller compared to adjacent regions to the target. Bolus thickness $b_{i,j}$ at a off axis-position (i,j), corrected for the bolus being non-water equivalent can be expressed as

$$b_{ij} = (1/\rho_b)\left[(R_t)_{ij} - d_{ij}\right] \tag{15}$$

where ρ_b is the effective density of the bolus material, d_{ij} is the depth of the distal target volume surface and the skin surface. In this equation the variation of therapeutic depth with off-axis position is included [22].

The isodose shift modification operator, $\mathbf{I}$, matches the distal surface of the target volume to an isodose contour that conforms 90% of the delivered dose. This operator can be expressed as $\mathbf{I} = \mathbf{I}(R_t)$ and is a one-dimensional operator. Initially, the dose distribution within the patient is calculated. Then, the point of intersection between every fan line

and the isodose surface is found. Next, the difference between the effective depth of the calculated points and the distal surface of the target volume is added or subtracted from the bolus thickness. Other three-dimensional operators are also calculated by using information from every fan line together with the adjacent fan lines in x- and y-directions. These operators are used for smoothing the bolus thickness, maximum coverage of target volume and maximum protection of organs at risk [22].

The creation operator will design the bolus along the fan lines that intersect with the target volume and will not consider the dose distribution along the field edges. To define the bolus outside the target volume and obtain the dose distribution along the field edges, the extension operators are needed. The bolus can be extended relative to the bolus thickness ($\mathbf{H}_t$) or the height ($\mathbf{H}_h$). To calculate $\mathbf{H}_h$, a rectangle encircling the bolus margin is defined. Next, the bolus surface height within this rectangle is calculated. The height at an off-axis position (i, j) is obtained with the following equation

$$h_{ij} = \sum_{m=1}^{4} \frac{(h_{kl})_m}{\rho_{ijkl}} \delta_m \left(\sum_{m=1}^{4} \frac{1}{\rho_{ijkl}} \delta_m \right)^{-1} \tag{16}$$

where h_{kl} is the harmonic mean of the nearest defined point along x- and y-directions, ρ_{ijkl} is the distance between the intersection point of isocenter plane and the fan line (i, j) and the intersection point of isocenter plane and the fan line (k, l). The sum over m is over the intersection lines drawn closest to the TVLM region along x-axis and y-axis, forming the rectangle. δ_m is equal to 1 if there is an intersection and 0 if there is no intersection. Using the harmonic mean the bolus is extended, by letting the surface positions be equal to the nearest point on the intersection lines, parallel to the x-axis and y-axis. The bolus is extended along the four corners of the rectangle [22].

The operators are useful for designing a bolus, however it is also necessary to compute the 3D dose distribution in the patient with bolus. This can done by incorporating the algorithms into a treatment planning system. [22].

When the design of the bolus is finished, it is fabricated. For this, machinable wax with linear stopping and scattering power close to polyethylene can be used. Utilizing a milling machine, the distal surface can be milled to match the patient surface and the proximal surface can be milled to conform the dose distribution [23].

A study by Kudchadker et al. demonstrated how a custom-made electron bolus can be used on patients with complex surface contour modification and patients with varying thickness of planing target volume (PTV) [24]. Two patients were treated. One patient had malignant fibrous histiocytoma on the right ear concha and received daily treatment with 12 MeV-electrons. The other patient had acinic cell carcinoma on the left parotid gland and received daily treatment with 20 MeV-electrons after complete removal of the parotid gland. For these patients with surgical defects, using a bolus as a substitute for the missing tissue was essential to avoid dose inhomogenity. Otherwise, there was a risk of underdosage of PTV leading to incomplete tumor response and a risk of increased side effects. Before producing a bolus, an approved treatment plan based on CT-images was needed. Subsequently, the production of the bolus was done by a milling machine that is

computer controlled. The resulting dose distribution was analyzed and it was concluded that 90% of the isodose on the surface was conformal to the PTV. The first patient received below 40 Gy to the brain, below 10 Gy to the spinal cord, and below 12 Gy to the right eye. The dose the first patient received to OAR was concluded to be minimal and below tolerance limits [24].

However, it is worth to mention that the increased surface dose caused erythema. The second patient received 60 Gy with a combined 20 MeV electron beam and 6 MV photon beam, in 27 fractions. Furthermore, this patient experienced severe skin reactions due to the bolus increasing the surface dose. The PTV received between 40-55 Gy which was better covered using a bolus. Moreover, the organs at risk received lower doses compared to a dose plan with no bolus. Additionally, the patients showed no signs of recurrence 6 months post-irradiation. Kudchadker et al. concluded that bolus is a useful method for conformal therapy, especially in cases with risk for inhomogeneities as mentioned in this study [24].

In another study by Perkins et al., custom-made 3D electron bolus were used on patients for postmastectomy irradiation. The bolus was designed to conform the 90% isodose surface to the surface of PTV. The bolus was produced by a computer controlled milling machine. The results were optimized dose distribution and reduced radiation to normal tissues. It was concluded that utilizing a custom-made 3D bolus increased dose homogeneity [25].

3 Material and Methods

3.1 Percentage Depth Dose Curves & Dose Profiles for SSD = 70 cm

The company .decimal requested percentage depth dose curves and dose profiles to make a designed model with settings specified for the modified linear accelerator used for FLASH-irradiation. For this, measurements were performed using films in a solid water phantom at an SSD = 70 cm, which is also the SSD used for the previously mentioned canine treatments. Firstly, the settings for FLASH-irradiation were chosen and a couple of dry runs were performed to make sure that the output from the linear accelerator was stable.

Next, EBT3 Gafchromic films, with dimensions 3.3 x 3.3 cm, were placed in the phantom at different depths to obtain percentage depth dose curves for different field sizes. Every measurement was repeated twice and the mean of the obtained data were calculated to reduce the effect of any output variation and/or difference in the response of individual pieces of film. For every irradiated film, there were two unirradiated film pieces kept that were from the same sheet to account for background.

The field size was controlled by placing a cerrobend block with an aperture with a certain diameter inside the applicator. For practical reasons, the films at different depths were divided into three sets and irradiated in three rounds. Similarly, the beam profiles for

different field sizes were measured by irradiating films at 2 cm depth in the solid water phantom. At each irradiation, 5 electron pulses were delivered, with 3 Gy/pulse. For a field size of d = 4 cm, the beam profile was also measured at 5 cm depth by placing a film at both 2 cm and 5 cm depth inside the solid water phantom. To obtain a response at 5 cm depth, 20 pulses were delivered instead of 5 pulses as for the previous measurements. Then, the gun current was lowered to conventional levels and a percentage depth dose curve and a beam profile at 2 cm were measured using the same setting as for FLASH-irradiation.
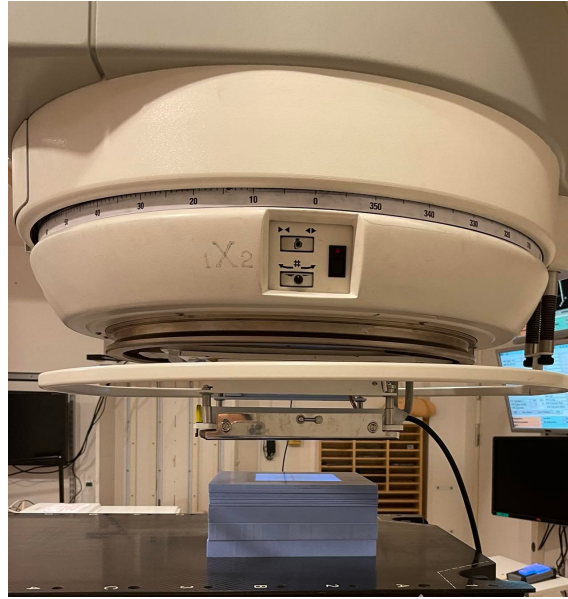
Figure 4: The setup for the measurements of percentage depth dose and dose profile. The solid water phantom is placed 5 cm beneath the tray. The applicator for SSD = 70 cm is also seen.

The irradiated and unirradiated films were scanned 24 h post-irradiation by placing the films, one piece at a time at, on the same position on a *Epson* scanner, using a scanning setting of 100 dots-per-inch. Next, using a program software called *ImageJ* the gray-scale values were obtained by defining a region of interest (ROI). Then, doses were calculated in *Excel* using the following previously obtained calibration equation.

$$D = -0.1603(I_0/I)^3 + 2.3384(I_0/I)^2 - 1.622(I_0/I) - 0.6728 \qquad (17)$$

where D is the absorbed dose in the film, I_0 is the gray scale value of unirradiated film and I is the gray scale value of irradiated film.

The measurements at different depths were used to calculated the relative doses at 10 mm to obtain a percentage depth dose curve. In some rounds, the films placed at 10 mm depth in the solid water phantom consisted of multiple films stacked on top of each other, hence the thickness of those films added to the actual depth. In these cases, to obtain the dose at 10 mm depth, polynomial regressions were performed. When the doses at 10 mm depth were obtained using the regressions, the doses in those rounds could be normalized

to the dose at 10 mm depth and be plotted.

The next step was to calculate the dose profiles. In ImageJ, a line ROI was defined both vertically and horizontally in every film to obtain the dose profile in both inline and crossline directions. For every ROI line, a profile with gray scale values as a function of distance in inches were received from the program. The data was imported into Excel. The gray scale values were converted into absorbed dose using the previously obtained calibration equation (Eq.(17)). The dose values were normalized to the mean of the values of the maximum dose. The x-axis was obtained by placing the origin in the center of the full-width-half-maximum. The distances in inches were converted to millimeters and the increment for every value was calculated and assigned to the x-axis to obtain the x-axis as the distance from the center of the beam.

Lastly, the beam dose profiles for 5 cm depth were related to the dose at 2 cm depth (obtained using 20 pulses). This was done by dividing the values of the dose profile at 5 cm with the maximum dose value at 2 cm depth.

Finally, this data could be sent to .decimal.

3.2 Percentage Depth Dose & Dose Profiles for SSD = 100 cm

When the company .decimal finished creating a model with parameters matching the modified linear accelerator, the treatment machine could be added to the software. However, the accuracy of this model was yet to be verified. During the initial measurements, an SSD of 70 cm was used, however due to a current limitation of the system software when choosing an SSD = 70 cm, an SSD of 100 cm had to be used for the time being. To compare the data from eRT software, new measurements were performed on the solid water and the Alderson phantom at SSD = 100 cm. Measurements at SSD = 70 cm were also performed on the Alderson phantom, intended to be compared later when the software is able handle an SSD of 70 cm.

To start to use the electron treatment planning system for FLASH-irradiation CT-images were acquired and structures were outlined. For this, imaging of the solid water and the Alderson phantom was performed. Next, using the contouring software in *Eclipse*, by *Varian*, structures such as body and a fictitious CTV were outlined. Thereafter, the images were imported into the eRT treatment planning system. Treatment plans were generated for the solid water phantom for different field sizes at SSD = 100 cm. Similarly, a dose plan was generated for the Alderson phantom for a field size with d = 5 cm at SSD = 100 cm. The field size in the software was chosen by adding a margin to CTV. Due to the CTV being at 2 cm depth in the solid water phantom and in the Alderson phantom, the field size had to be chosen larger to have the correct field size at SSD = 100 cm. To determine the exact field size at 2 cm depth, the full-width-half-maximum (FWHM) of the profiles at 2 cm depth in the solid water phantom and Alderson phantom were calculated using the measured data.

When the plans had been generated in the eRT software, the beam data could be ex-

ported. Using ImageJ and Excel, the percentage depth dose curves and profiles for the solid water phantom and profiles for the Alderson phantom were obtained from the dose distribution that the software had computed.

Lastly, those plans were verified by measurements on the solid water and Alderson phantom. Measurements of percentage depth dose curve and dose profile were performed on the solid water phantom for different field sizes at SSD = 100 cm. Previously, an applicator suited for SSD = 70 cm with an inserted transmission chamber was used. For measurements with SSD = 100 cm, the applicator had to be changed. The source-tray distance, STD, was also changed from 65 cm to 95 cm.
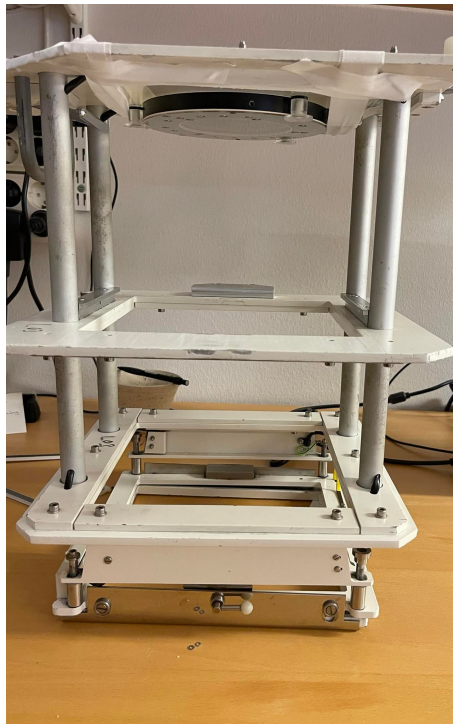
Figure 5: The 20x20 cm applicator for SSD = 100 cm.

Instead of placing the films at different depths for measuring the percentage depth dose curve, a single film was sandwiched between blocks of 4 cm on each side of the film (see Figure 6). The film together with the blocks were placed on the couch and a gantry angle of 2° was used. A dose profile was also measured by placing a film at 2 cm depth inside the solid water phantom. The measurements of the solid water phantom were repeated for three different field sizes with diameters of 3, 5 and 8 cm. Next, the dose profile of the Alderson phantom was measured similarly by placing a film at 2 cm depth, using a field size with a diameter of 5 cm (see Figure 7).
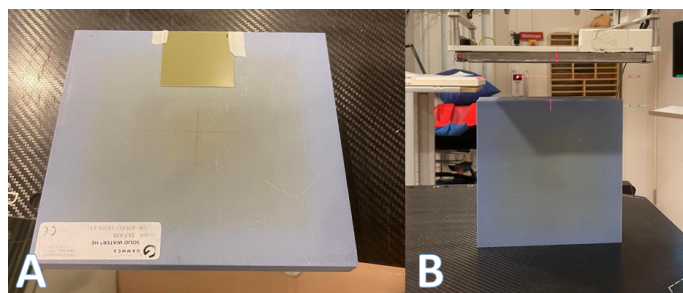
Figure 6: The setup for measurements of percentage depth dose in the solid water phantom. In A, the film was taped to the phantom and in B the film is sandwiched between the blocks and placed with the width perpendicular to the lateral direction underneath the applicator.
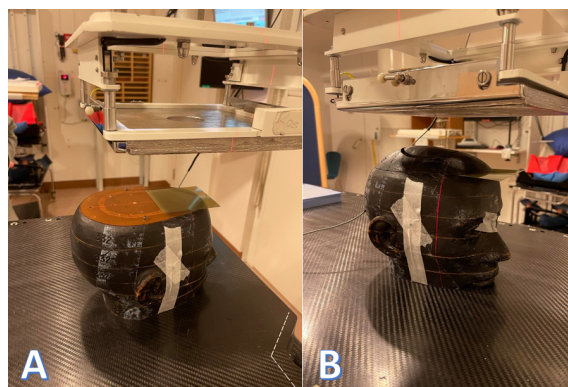
Figure 7: The setup for measurements of dose profile in the Alderson phantom. In A, the phantom is positioned using the in-room isocenter lasers. In B, the 2 cm top piece of the phantom has been re-attached to the phantom and the distance between the top surface of the phantom and the tray was set to 5 cm.

The films were scanned 24 h post-irradiation and imported to Excel after obtaining the gray scale values from ImageJ. The percentage depth dose was corrected for the gantry angle of $2°$ and the relative doses were calculated. The dose profiles obtained from the measurements were also calculated as done previously. The exported data from eRT was and compared with the measurements in Excel.

3.3   FLASH-irradiation using Custom-made Bolus

To reduce the inhomogeneity in dose distribution and the dose to the bone, an optimized thickness bolus was added to the Alderson-phantom plan in the treatment planning system eRT. The TPS performed the optimization of the bolus thickness using the bolus design algorithms.
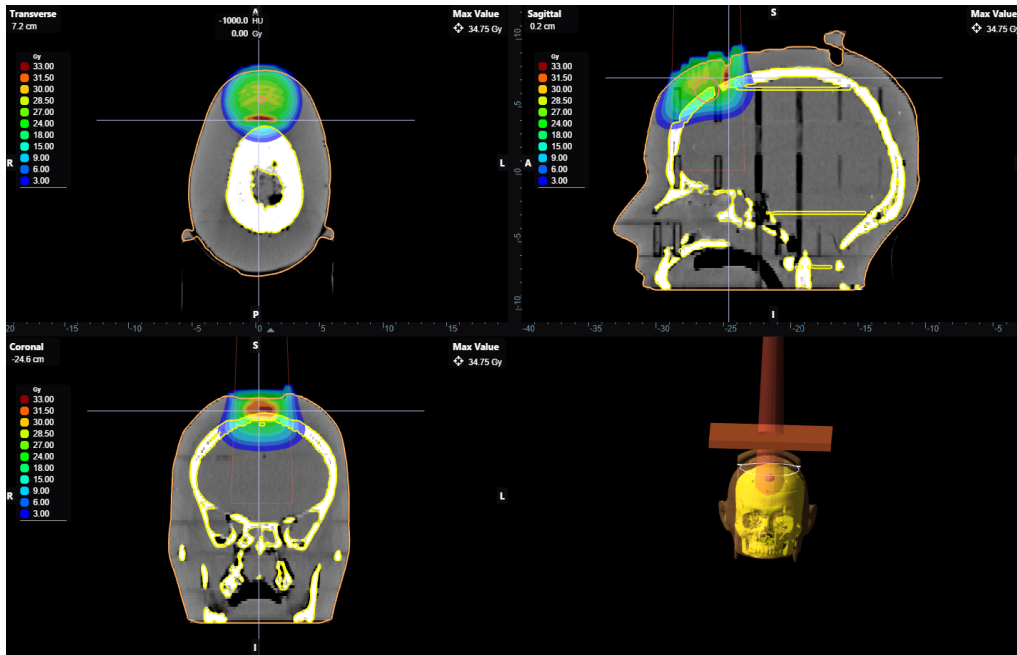
Figure 8: The initial treatment plan without optimized thickness bolus. Here an SSD = 100 cm and a field size with a diameter of 5 cm were used.
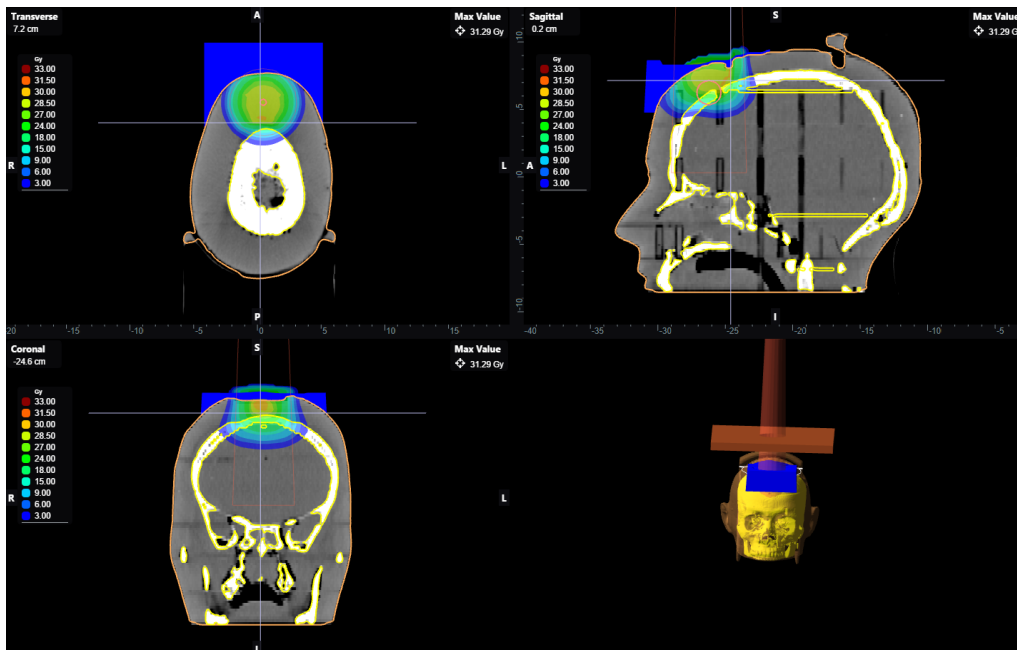
Figure 9: The treatment plan with an optimized thickness bolus.

The eRT-TPS uses a copper block to collimate the field size, seen in Figure 9, which can also be ordered together with the bolus. Following plan approval, the bolus and the copper block were ordered from within the TPS-software.

When the bolus and the block arrived, the same setup as in section 3.2 was repeated, see

Figure 10. The copper block with d = 5 cm was placed inside the 20x20 cm applicator, where the cerrobend block was placed previously (seen in Figure 5).
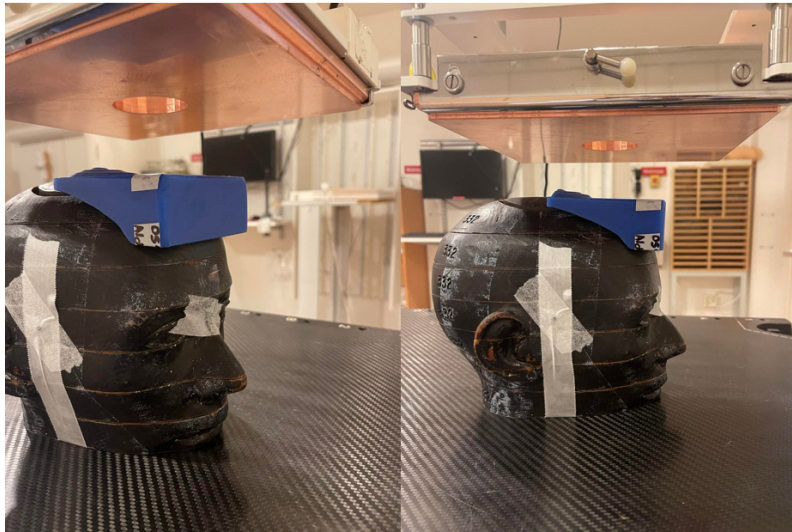
Figure 10: The setup for measurement of dose profile in the Alderson phantom with an optimized thickness bolus. The copper block with an aperture with a diameter of 5 cm is also seen.
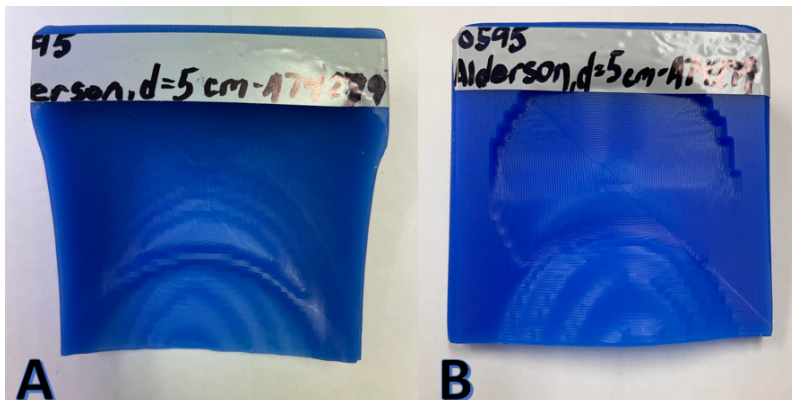
Figure 11: The bolus used on the Alderson phantom. A: the inner side of the bolus which is milled to match the surface of the Alderson phantom. B: the top which faces the copper block in Figure 10.

A film was placed inside the Alderson phantom at 2 cm depth and the bolus was placed on top. Next, 5 electron pulses were delivered with 3 Gy/pulse.

At 24 h post-irradiation, the films together with the corresponding unirradiated films were scanned, as done before, using the Epson scanner. The obtained gray values were converted to absorbed dose using Eq.(17). Next, the exported data of the dose plan for the bolus was compared with the measurements.

4 Results

4.1 Percentage Depth Dose & Dose Profiles for SSD = 70 cm

The percentage depth dose curves in the solid water phantom for a field size with a diameter of 2 cm can be seen in Figure 12. The percentage depth dose curves for other field sizes can be seen in the Appendix section. All percentage depth dose curves were normalized to the dose at 10 mm depth. As mentioned in the Method section, the films were irradiated in three rounds and divided into three sets. The sets included films placed at different depths. Set 1 included the depths 1, 3.3, 5.6, 10.8, 16.1, 21.4, 41.7 mm for field sizes d = 2, 3, 4, 6 and 8 cm and the field size 10 x 10 cm. Set 2 included the depths 10, 30.3, and 50.6 mm for field sizes d = 2, 3, 4, 6 and 8 cm and the field size 10 x 10 cm. Set 3 included the depths 7, 10.3, 12.6 and 24.8 for the field size d = 2 cm. For field size d = 3, set 3 included the depths 10, 12.3, 17.6 and 24.8 mm. For field sizes d = 4, 6, 8 and the field size 10 x 10 cm, set 3 included the depths 10, 17.3, 22.6 and 24.8 mm. Some of these sets had films placed at a shallower depth than 10 mm, hence adding to the actual depth at 10 mm. Thus, polynomial regressions were performed to find the dose at depth 10 mm for those sets. The polynomial regressions can be found in the Appendix section.
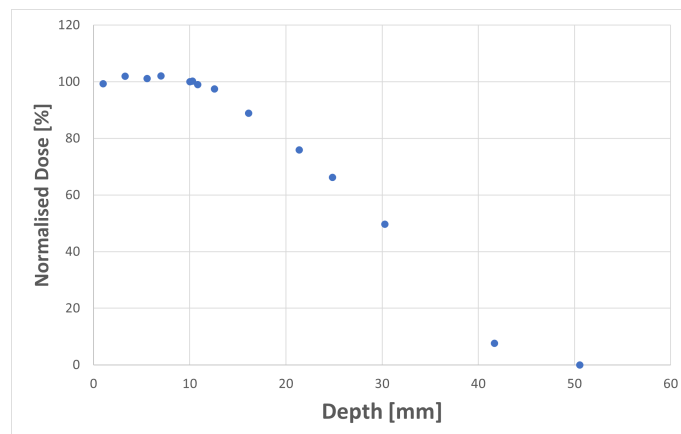
Figure 12: The percentage depth dose curve for a field size with d = 2 cm. The value at the depth 5 cm is seen as zero due to the film not being able to detect the small dose levels at that depth with the number of pulses given.

In Figure 13, the comparison between the percentage depth dose curves, measured with ultra-high dose rate and conventional dose rate, respectively, can be seen.
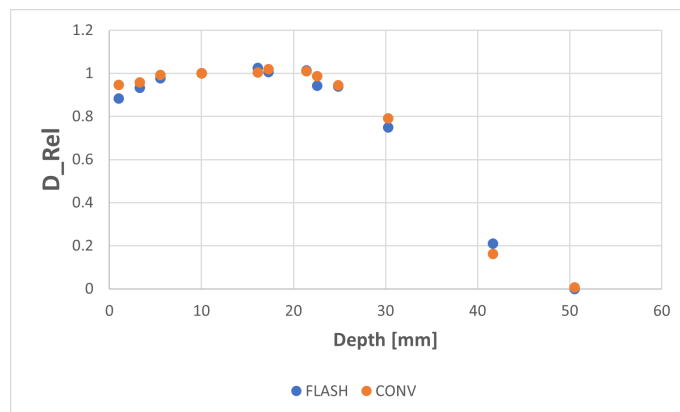
Figure 13: The percentage depth dose curves for field size with d=4 cm, measured with ultra-high (FLASH) and conventional (CONV) dose rates.

The deviations between the repeated measurements for different depths were computed in Excel. Measurements of the field size with a diameter of 3 cm had the largest deviation values, see Table 1. In the Appendix-section, the tables with deviation values for other field sizes can be found.

Table 1: The deviations between the twice repeated measurements for different depths and field size d = 3 cm. NA = not available.

Depth [mm]	Deviation [%]
1	3.4
3.3	0.2
5.6	3.3
12.3	3.1
16.1	5.6
17.6	1.3
21.4	1.5
24.8	2.1
30.3	0.2
41.7	0.7
50.6	NA

In Figure 14, a dose profile for the field size with a diameter of 2 cm can be seen, in both inline and crossline directions. The dose profiles for other field sizes can be found in the Appendix section. The measurements were performed at 2 cm depth in the solid water phantom. It can be seen that the two profiles in crossline and inline direction are overlapping. This shows that our beam is symmetrical and Gaussian. The profiles were normalized to the mean of maximum values.
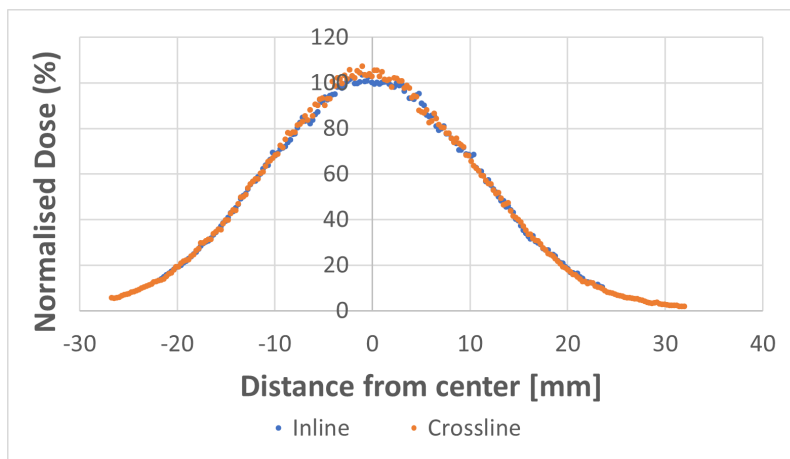
Figure 14: Dose profile at 2 cm depth, in inline and crossline directions for a field with d = 2 cm.

Figure 15 shows the dose profile at 5 cm normalized to the maximum value of the dose profile at 2 cm. The maximum value of the beam dose profile at 2 cm was obtained from the same measurement as for the profile at 5 cm. In Figure 15, it can be seen that at the depth 5 cm, which is beyond the practical range of the electrons, there is 3 % dose at the beam center relative to the dose at 2 cm depth which corresponds to the bremsstrahlung tail.
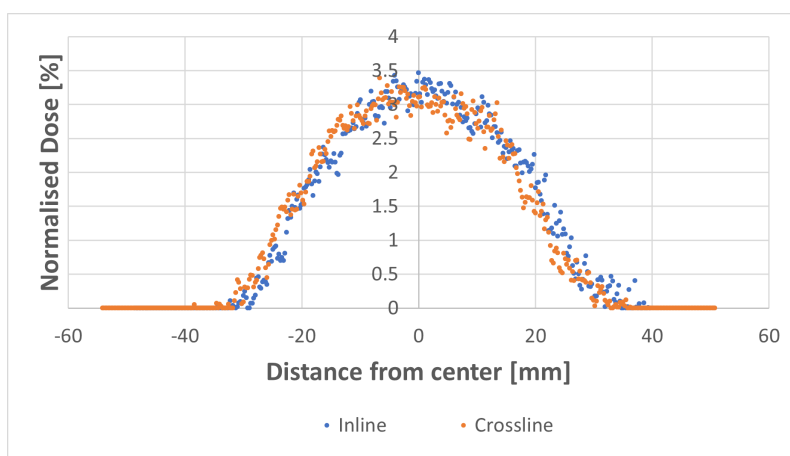
Figure 15: Dose profile at 5 cm normalized to the maximum dose profile value at 2 cm.

The comparison between the dose profiles measured with ultra-high and conventional dose rates does not show any great visual differences, see Figure 16.
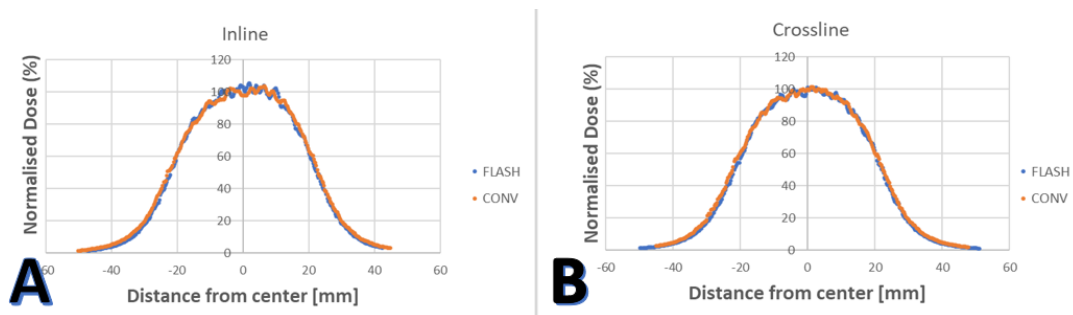
Figure 16: Dose profiles at 2 cm depth in crossline (A) and inline (B) directions for a field size with d = 4 cm. The profiles are measured using ultra-high (FLASH) and conventional (CONV) dose rate, respectively.

4.2   Percentage Depth Dose & Dose Profiles for SSD = 100 cm

The percentage depth dose curves are normalized to its maximum value. The curves were shifted on the x-axis such that x=0 is at the surface of the phantom, see Figure 17.
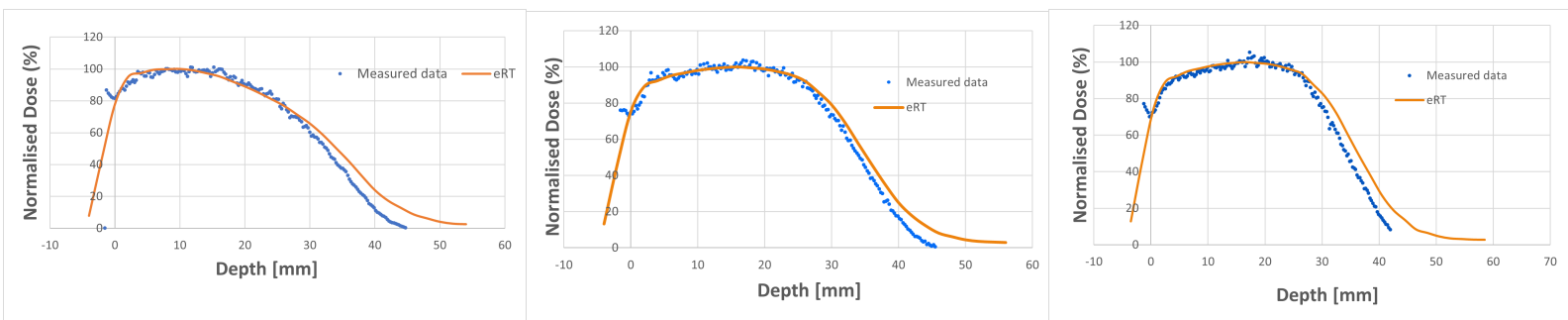
(a) Percentage depth dose curves for the field size with diameter of 3 cm.

(b) Percentage depth dose curve for the field size with diameter of 5 cm.

(c) Percentage depth dose curve for the field size with diameter of 8 cm.

Figure 17: Percentage depth dose curves measured in the solid water phantom and computed in the eRT-TPS.

In Figure 18, the dose profiles were measured at 2 cm depth in the solid water phantom and the curves are normalized to its maximum value.
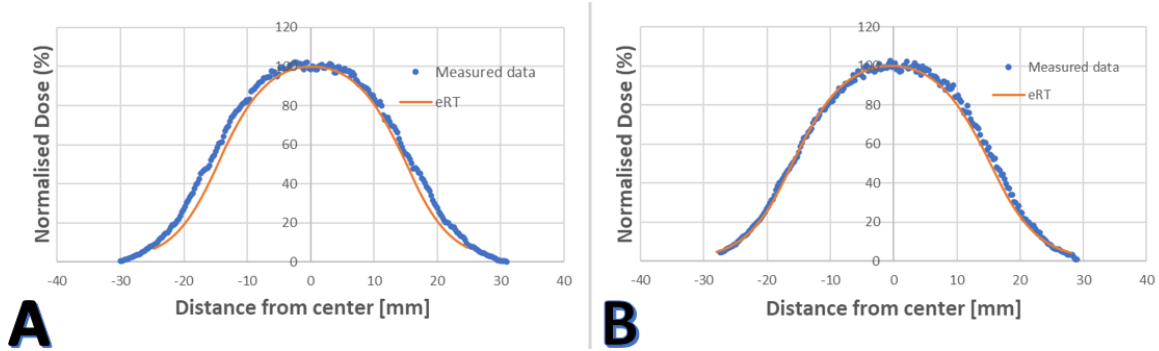
(a) Dose profiles for the field size with diameter of 3 cm.
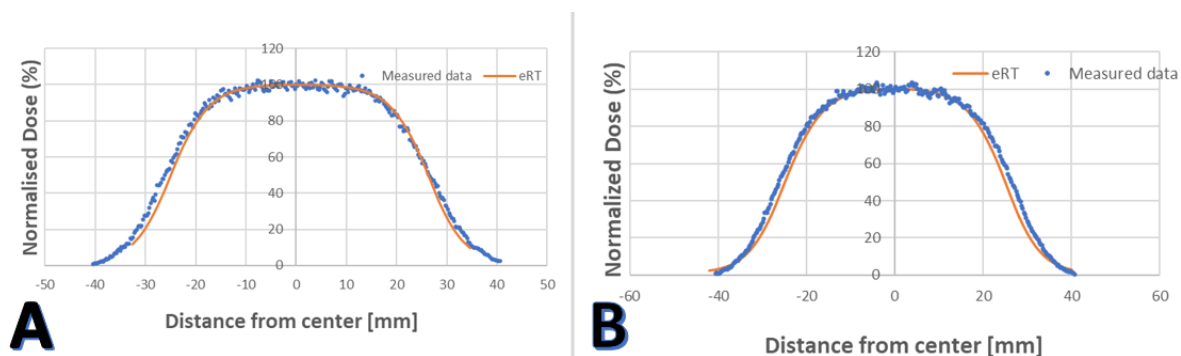
(b) Dose profiles for the field size with diameter of 5 cm.
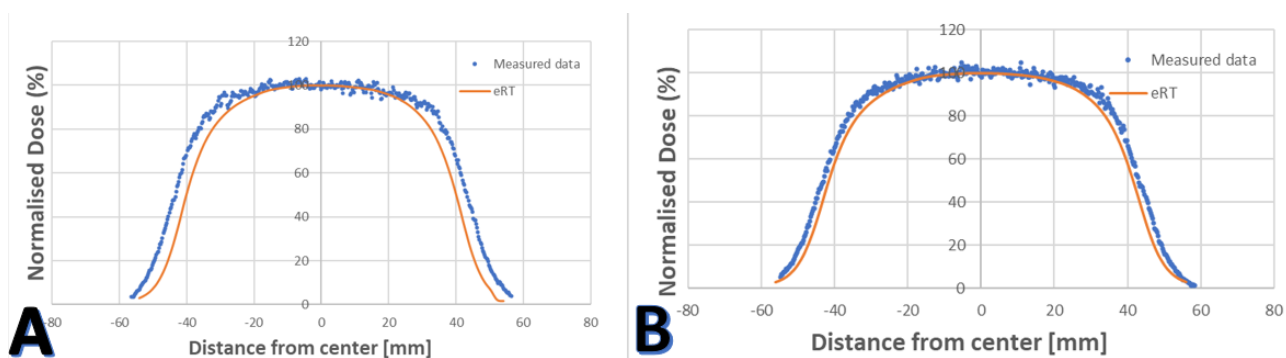
(c) Dose profiles for the field size with diameter of 8 cm.
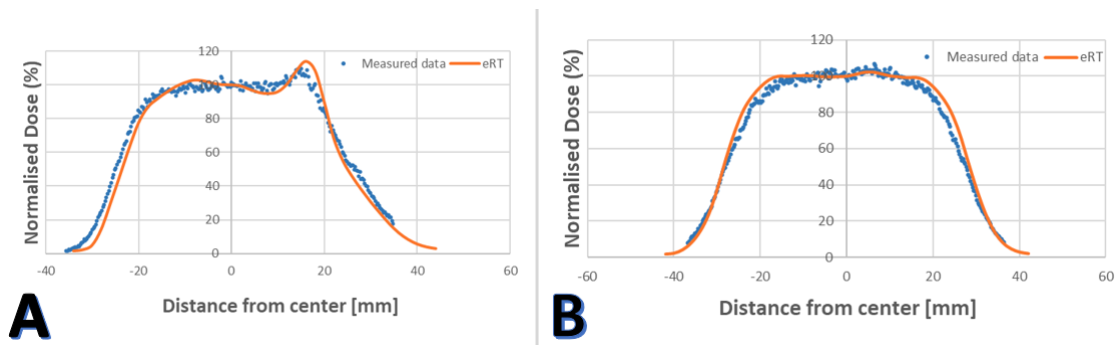
Figure 18: Dose profiles obtained by film measurements and exported data from eRT TPS. A: Inline dose profile. B: Crossline dose profile.

In Figure 19, the dose profiles were measured at 2 cm depth in the Alderson phantom and the curves are normalized to the central axis. Both in the measured inline dose profile and the computed inline dose profile a peak was observed with $\approx 15\%$ higher dose.

Figure 19: Dose profiles obtained by film measurements and exported data from eRT-TPS, for a field size with d = 5 cm. A: Inline dose profile. B: Crossline dose profile.

The deviations between the full-width at half-maximum of the measured and computed dose profiles were obtained in Excel. The largest deviation can be seen for the inline dose profile with a field size of a diameter equal to 8 cm, see Table 2.

Table 2: The deviation between the FWHM-values of the dose profiles for crossline and inline directions in the solid water and the Alderson phantom.

Field size [cm]	Deviation [%] (Crossline)	Deviation [%] (Inline)
d = 3	0.4	2.8
d = 5	2.5	1.5
d = 8	1.4	3.2
d = 5 (Alderson)	0.1	3.0

Furthermore, using gamma analysis the passing rates for the obtained dose distributions were computed with the acceptance criteria of 2 mm DTA (distance to agreement) and 2% DD (dose difference). In Table 3, it can be seen that the dose distribution from the dose profile for the field size d = 8 cm have the lowest passing rates.

	Field Size	Passing Rate (2 mm, 2%) (inline/crossline)
Dose Profile	d =3	95.8/ 96.9%
	d = 5	88.0/91.2 %
	d = 8	36.0/ 62.8 %
	d = 5 (Alderson)	81.8/ 75.5 %
Percentage Depth Dose	d =3	76.8 %
	d = 5	84.6 %
	d = 8	71.0 %

Table 3: Passing rates with gamma criteria of 2 mm and 2 % for dose distributions obtained from percentage depth dose and dose profile (inline/crossline) measurements in the solid water and the Alderson phantom.

4.3   Dose Profiles with Bolus for SSD = 100 cm

In Figures 20-21, the dose profiles at 2 cm depth with bolus in the Alderson phantom are seen. The curves are normalized to its central axis. The deviation between the FWHM of

the dose profiles in the inline and the crossline direction is 0.5% and 1.5%, respectively. The gammas passing rate with the acceptance criteria of 2 mm DTA and 2% DD is 72.9 % and 92.6 % for the dose distribution in inline and crossline direction, respectively. The hot spot previously observed in inline dose profile with no bolus (Figure 19A) is not observed in the inline dose profile with bolus (Figure 21).
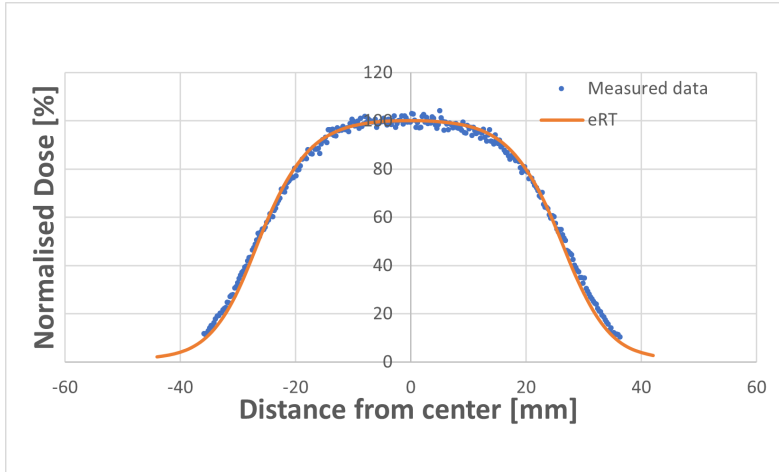

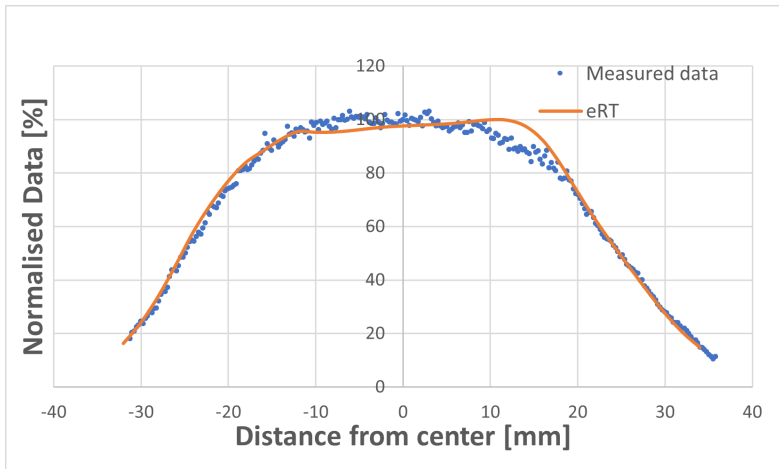
Figure 20: The dose profile at 2 cm depth with bolus, in the crossline direction.

Figure 21: The dose profile at 2 cm depth with bolus, in the inline direction.

5 Discussion

5.1 Percentage Depth Dose & Dose Profiles for SSD = 70 cm

It can be seen in Figures 12 and S1-S5 how z_{max} is increased with increased field size, which was expected from the theory. However, in the PDD-curve in Figure S1, PDD-values had large deviations between the identical repeated measurements, see Table 1. According to Sorriaux et al., the EBT3 single film reproducibility is ensured with a standard deviation <0.01% (as mention in the theory section), which indicates that the deviation values seen in Table 1 may be caused by beam issues. However, this could also be

caused by a poor film sheet or errors in managing the films and further measurements are required. Consequently, the PDD-curve and the beam dose profile for field size with d = 3 cm were excluded from the data sent to .decimal.

There is no difference observed in the PDD-curves (Figure 13) and the dose profiles (Figure 16) using the modified linear accelerator with ultra-high and conventional dose rates. This was expected because the PDD-curves and beam dose profiles are independent of the dose rate. The comparisons in Figures 13 and 16 were only done for verification and were not part of the data that were sent to .decimal.

In Figures 14 and S12-S16, an increase of the dose profile width can be seen with increased field size. The crossline and inline profiles overlap in the solid water phantom, which confirms that our beam is symmetrical and Gaussian in shape. A small difference is seen in Figure S16, which could be caused by noise. Nevertheless, the profiles are not flat as the example illustrated in the Theory section (Figure 2). The reason behind this is that the modified linear accelerator has the primary and the scattering foils removed to reach ultra-high dose rates, causing the beam profiles to be unflattened. In the future, if it becomes possible to use more radiation intense sources to obtain the ultra-high dose rates, the dual foil scattering system may be used to flatten the dose profiles.

According to the manufacturer of Gafchromic EBT3 film the optimum dose range is between 0.2 to 10 Gy. Hence the profile at the depth 5 cm was measured using 20 pulses because the dose was to small to be distinguished at the depth 5 cm using 5 pulses. Due to the low dose beyond the practical range of electrons at depth 5 cm, a lot of noise is seen in Figure 15. In Figure 15 it can be seen that 3% of the dose at 2 cm depth is left at 5 cm depth. The bremstrahlung tail is expected to be in the order of a few percent, thus the value of 3% seems reasonable.

5.2   Percentage Depth Dose & Dose Profiles for SSD = 100 cm

In Figure 17, good agreement can be seen between the measured percentage depth dose values and the data exported from the eRT-TPS. The calculation model in TPS is based on the initial measurements that were sent to *.decimal*. The initial measurements were performed using an applicator suited for SSD = 70 cm (see Figure 4), which is the applicator incorporated to the TPS. For the measurements in section 3.2 an applicator for SSD = 100 cm was used (see Figure 5), which is not incorporated to the TPS. As mentioned in the Theory section, the applicator in use should be incorporated into the TPS. Due to different applicators being used, the accuracy may not be as good as expected and the scattered radiation may not be included completely accurately. Therefore, redoing the measurements using the applicator for SSD = 70 cm, or including the applicator for SSD = 100 cm to the TPS, more accurate results may be obtained and the passing rates seen in Table 3 may be improved. Regardless, the fact that different applicators were used to obtain the results, a good agreement can still be observed in section 4.2. The observed deviation between the curves, in Figure 17, at larger depths (beyond x= 40 mm), is likely due to the limitations in the films characteristics. As mentioned previously small doses beneath 0.2 Gy cannot

be detected. Thus one alternative could be to increase the number of delivered pulses to increase the minimum dose. However, the maximal dose must also be considered which will increase with increased number of pulses, as the optimum dose range is up to 10 Gy.

The dose profiles in Figures 18 and 19 also show great accordance between the measured data and exported data from eRT-TPS, with a deviation of FWHM not higher than 3% (except Figure 18c). The dose profiles with the field size d = 8 cm have the largest deviations and the lowest passing rates and the differences are also seen in Figure 18c. The effect of using different applicators and thus the incorrectly inclusion of scattered radiation is noticed more for larger field sizes. It is also worth to mention the peak seen in Figure 19A caused by a hot spot in the Alderson phantom. The hot spot is caused by small cavities in the construction of the Alderson phantom. In the hot spot, the dose is increased by 15 % which will have a great impact, especially since FLASH is usually delivered with fewer fractions and thus with a high fraction dose.

5.3   Dose Profiles with Bolus for SSD = 100 cm

Dose profiles at 2 cm depth in the Alderson phantom were measured using a custom-made bolus. The expected dose distribution from the TPS can be seen in Figure 9, which were exported and plotted together with the measured dose profiles (see Figures 20 and 21). In Figure 20, accordance in crossline direction can be seen between the measured data and the exported data from eRT, with a passing rate of 92.6 %. However, in the inline direction (Figure 21) a difference of 5% can be seen for x = -10 mm to x = -4 mm, and for x = 10 mm to x = 16 mm a difference of 10% can be seen. The data from eRT shows a more flattened profile in inline direction compared to the obtained measured data, resulting in differences seen in Figure 21. This could be caused by difficulties in placing the bolus correctly on top of the Alderson phantom and further measurements need to be performed to confirm the accuracy of the data from the eRT-TPS. However, the deviation values are below 2% and the passing rate is 72 %. The hot spot observed in Figure 19A seems to have disappeared, thus it seems like using custom-made bolus to make treatments more conformal is promising with a more homogeneous dose distribution obtained.

6   Conclusions

The eRT-TPS system by *.decimal* was evaluated by phantom measurements. Initially, the goal was to compare computed data with phantom measurements at an SSD of 70 cm, however due to a current limitation of the system an SSD of 100 cm had to be used instead. Though good agreement could be seen in the results, deviations due to the comparison of phantom measurements at an SSD 100 cm and computed data from eRT, that is based on an SSD 70 cm, could be observed. This effect was particularly noticed for larger field sizes with lower gamma passing rates. Thus, for the verification of the eRT-TPS, an evaluation at an SSD 70 cm needs to be performed. The use of an optimized thickness bolus resulted in the disappearance of a hot spot and it seems promising for obtaining more conformal veterinary treatments in the future, although further measurements are needed to confirm the accuracy of the bolus optimization in the eRT-TPS.

7   Acknowledgments

First of all, I would like to thank my supervisors *Crister Ceberg*, *Elise Konradsson* and *Kristoffer Petersson* for giving me the opportunity to work on this project. I have gained valuable experience that will help me throughout my career.

I want to thank my friends, sisters, and brother for always cheering me up and putting a smile on my face. You guys are funny even when you are not.

Lastly and most importantly, I want to thank my parents for raising me up to the person I am today - *älskar er*.

8   References

References

[1] Favaudon, V., Caplier, L., Monceau, V., Pouzoulet, F., Sayarath, M., Fouillade, C., Poupon, M., Brito, I., Hupé, P., Bourhis, J., Hall, J., Fontaine, J. and Vozenin, M., 2014. Ultrahigh dose-rate FLASH irradiation increases the differential response between normal and tumor tissue in mice. Science Translational Medicine, 6(245).

[2] Vozenin, M., De Fornel, P., Petersson, K., Favaudon, V., Jaccard, M., Germond, J., Petit, B., Burki, M., Ferrand, G., Patin, D., Bouchaab, H., Ozsahin, M., Bochud, F., Bailat, C., Devauchelle, P. and Bourhis, J., 2018. The Advantage of FLASH Radiotherapy Confirmed in Mini-pig and Cat-cancer Patients. Clinical Cancer Research, 25(1), pp.35-42.

[3] National Cancer Institute. 2018. External Beam Radiation Therapy for Cancer. [online] Available at: <https://www.cancer.gov/about-cancer/treatment/types/radiation-therapy/external-beam> [Accessed 20 December 2021].

[4] Bourhis, J., Sozzi, W., Jorge, P., Gaide, O., Bailat, C., Duclos, F., Patin, D., Ozsahin, M., Bochud, F., Germond, J., Moeckli, R. and Vozenin, M., 2019. Treatment of a first patient with FLASH-radiotherapy. Radiotherapy and Oncology, 139, pp.18-22.

[5] Konradsson, E., Arendt, M., Bastholm Jensen, K., Børresen, B., Hansen, A., Bäck, S., Kristensen, A., Munck af Rosenschöld, P., Ceberg, C. and Petersson, K., 2021. Establishment and Initial Experience of Clinical FLASH Radiotherapy in Canine Cancer Patients. Frontiers in Oncology, 11.

[6] Wilson, J., Hammond, E., Higgins, G. and Petersson, K., 2020. Ultra-High Dose Rate (FLASH) Radiotherapy: Silver Bullet or Fool's Gold?. Frontiers in Oncology, 9.

[7] Podgorsak, E., 2005. Radiation oncology physics. Vienna: International Atomic Energy Agency.

[8] Podgorsak, E., 2012. Chapter 8: Electron Beams: Physical and Clinical Aspects. [online] Www-naweb.iaea.org. Available at: <http://www-naweb.iaea.org/nahu/DMRP/documents/slides/Chapter_08 _Electron_beams.pdf> [Accessed 16 November 2021].

[9] LeBlanc, J., 2012. Design of electron dual foil scattering systems for Elekta Infinity radiotherapy accelerators. [online] LSU Digitalcommons. Available at: <https://digitalcommons.lsu.edu/cgi/viewcontent.cgi?article=3439 &context=gradschool_theses> [Accessed 22 December 2021].

[10] Battum, L., Zee, W. and Huizenga, H., 2003. Scattered radiation from applicators in clinical electron beams. Physics in Medicine and Biology, 48(15), pp.2493-2507.

[11] Lempart, M., Blad, B., Adrian, G., Bäck, S., Knöös, T., Ceberg, C. and Petersson, K., 2019. Modifying a clinical linear accelerator for delivery of ultra-high dose rate irradiation. Radiotherapy and Oncology, [online] 139, pp.40-45. Available at: <https://doi.org/10.1016/j.radonc.2019.01.031>.

[12] Konradsson, E., Ceberg, C., Lempart, M., Blad, B., Bäck, S., Knöös, T. and Petersson, K., 2020. Correction for Ion Recombination in a Built-in Monitor Chamber of a Clinical Linear Accelerator at Ultra-High Dose Rates. Radiation Research, 194(6).

[13] Burnet, N., 2004. Defining the tumour and target volumes for radiotherapy. Cancer Imaging, 4(2), pp.153-161.

[14] TASCHETTA-MILLANE, M., 2016. Treatment Planning Systems Overview. [online] Imaging Technology News. Available at: <https://www.itnonline.com/article/treatment-planning-systems-overview> [Accessed 3 November 2021].

[15] Shiu, A. and Hogstrom, K., 1991. Pencil-beam redefinition algorithm for electron dose distributions. Medical Physics, 18(1), pp.7-18.

[16] De Martino, F., Clemente, S., Graeff, C., Palma, G. and Cella, L., 2021. Dose Calculation Algorithms for External Radiation Therapy: An Overview for Practitioners. Applied Sciences, 11(15), p.6806.

[17] Oelkfe, U. and Scholz, C., 2006. New technologies in radiation oncology. Berlin: Springer.

[18] Hogstrom, K., Mills, M. and Almond, P., 1981. Electron beam dose calculations. Physics in Medicine and Biology, 26(3), pp.445-459.

[19] Jaccard, M., Petersson, K., Buchillier, T., Germond, J., Durán, M., Vozenin, M., Bourhis, J., Bochud, F. and Bailat, C., 2017. High dose-per-pulse electron beam dosimetry: Usability and dose-rate independence of EBT3 Gafchromic films. Medical Physics, 44(2), pp.725-735.

[20] Butson, M., Yu, P., Cheung, T. and Metcalfe, P., 2003. Radiochromic film for medical radiation dosimetry. Materials Science and Engineering: R: Reports, 41(3-5), pp.61-120.

[21] Sorriaux, J., Kacperek, A., Rossomme, S., Lee, J., Bertrand, D., Vynckier, S. and Sterpin, E., 2013. Evaluation of Gafchromic® EBT3 films characteristics in therapy photon, electron and proton beams. Physica Medica, 29(6), pp.599-606.

[22] Low, D., Starkschall, G., Bujnowski, S., Wang, L. and Hogstrom, K., 1992. Electron bolus design for radiotherapy treatment planning: Bolus design algorithms. Medical Physics, 19(1), pp.115-124.

[23] Hogstrom, K., Antolak, J., Kudchadker, R., Ma, C. and Leavitt, D., 2003. Modulated Electron Therapy. [ebook] Available at: <https://dotdecimal.com/wp-content/uploads/2015/10/Hogstrom-et-al-AAPM-SS-2003-Modulated-Electron-Therapy.pdf> [Accessed 23 December 2021].

[24] Kudchadker, R., Antolak, J., Morrison, W., Wong, P. and Hogstrom, K., 2003. Utilization of custom electron bolus in head and neck radiotherapy. Journal of Applied Clinical Medical Physics, 4(4), p.321.

[25] Perkins, G., McNeese, M., Antolak, J., Buchholz, T., Strom, E. and Hogstrom, K., 2001. A custom three-dimensional electron bolus technique for optimization of postmastectomy irradiation. International Journal of Radiation Oncology*Biology*Physics, 51(4), pp.1142-1151.
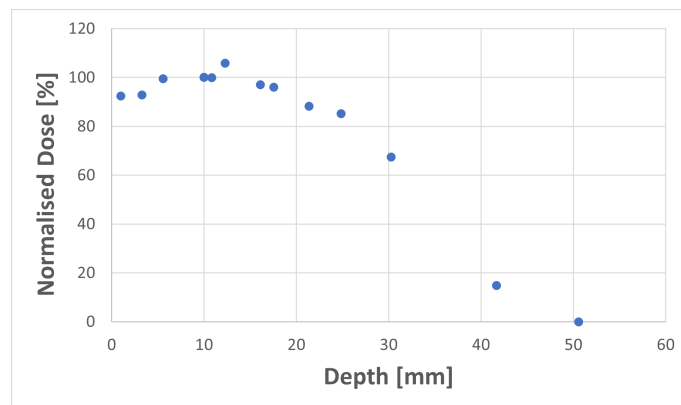
9 Appendix

Figure S1: The percentage depth dose curve for a field size with d = 3 cm. The value at the depth 5 cm is seen as zero due to the film not being able to detect the small dose levels at that depth with the number of pulses given.
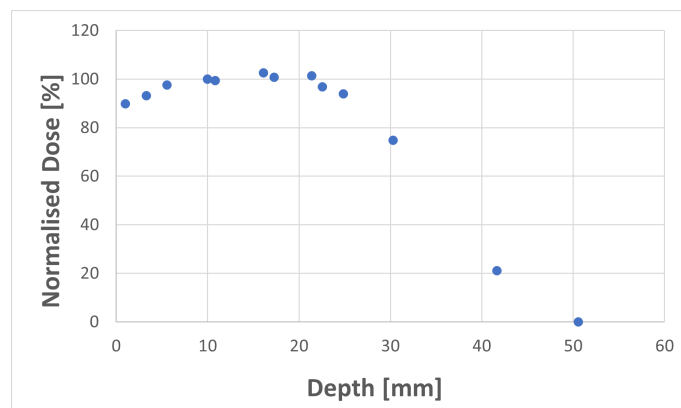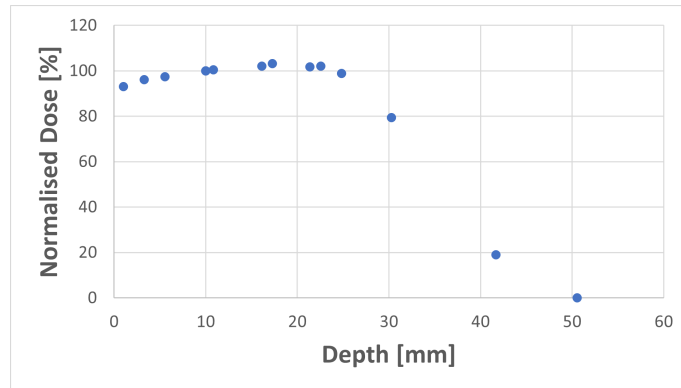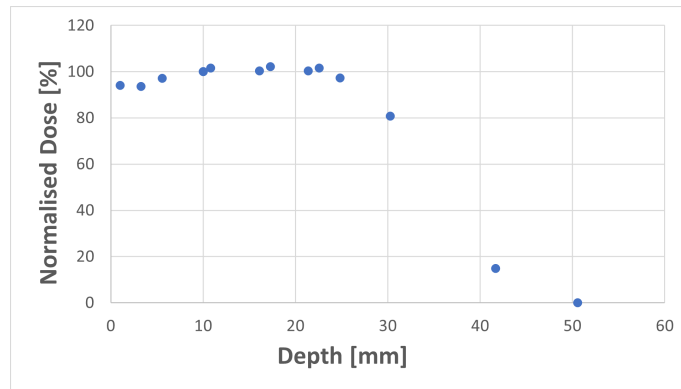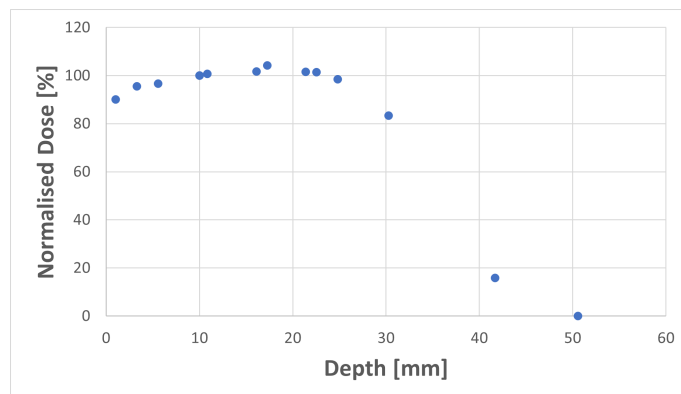

Figure S2: The percentage depth dose curve for a field size with d = 4 cm. The value at the depth 5 cm is seen as zero due to the film not being able to detect the small dose levels at that depth with the number of pulses given.

Figure S3: The percentage depth dose curve for a field size with d = 6 cm. The value at the depth 5 cm is seen as zero due to the film not being able to detect the small dose levels at that depth with the number of pulses given.

Figure S4: The percentage depth dose curve for a field size with d = 8 cm. The value at the depth 5 cm is seen as zero due to the film not being able to detect the small dose levels at that depth with the number of pulses given.

Figure S5: The percentage depth dose curve for a field size with dimensions 10x10 cm. The value at the depth 5 cm is seen as zero due to the film not being able to detect the small dose levels at that depth with the number of pulses given.
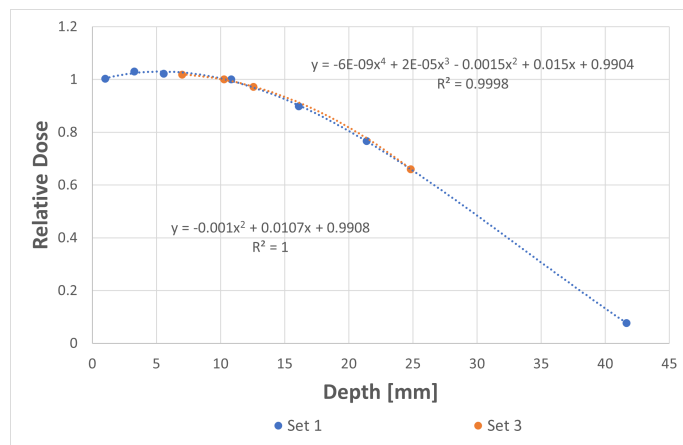
Figure S6: The regressions for set 1 and set 3 together with the corresponding equations used to find the dose at 10 mm depth, for a field size with a diameter of 2 cm.
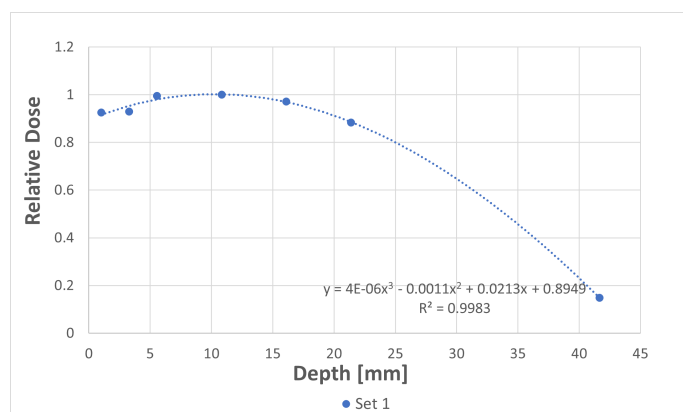
Figure S7: The regression for set 1 together with the corresponding equation used to find the dose at 10 mm depth , for a field size with a diameter of 3 cm.
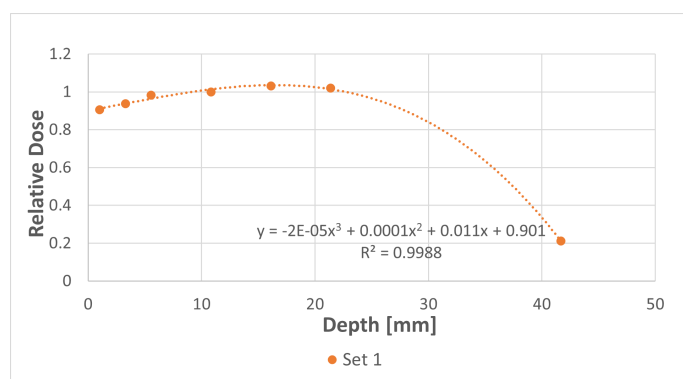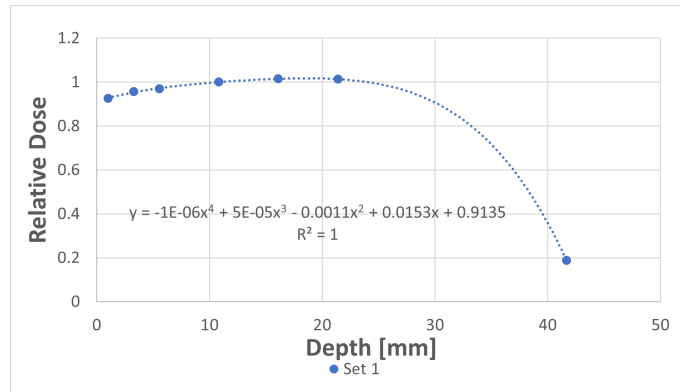

Figure S8: The regression for set 1 together with the corresponding equation used to find the dose at 10 mm depth, for a field size with a diameter of 4 cm.

Figure S9: The regression for set 1 together with the corresponding equation used to find the dose at 10 mm depth, for a field size with a diameter of 6 cm.
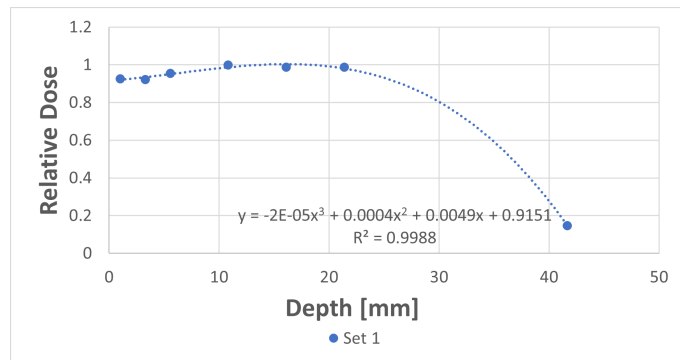

Figure S10: The regression for set 1 together with the corresponding equation used to find the dose at 10 mm depth, for a field size with a diameter of 8 cm.
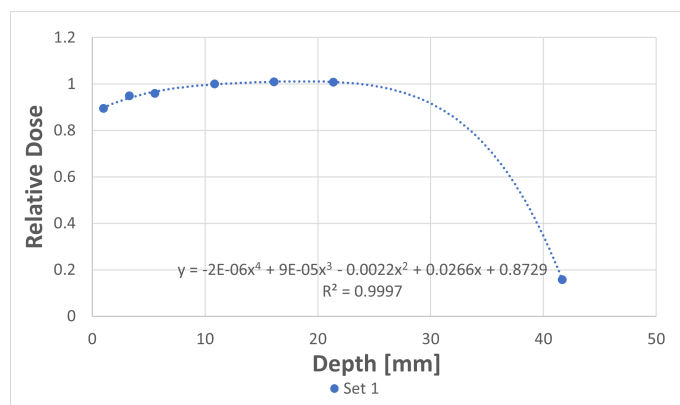

Figure S11: The regression for set 1 together with the corresponding equation used to find the dose at 10 mm depth, for a field size with dimensions 10x10 cm.

Table S1: The deviations between the twice repeated measurements for different depths and field size d = 2 cm. NA = not available.

Depth [mm]	Deviation [%]
1	1.7
3.3	1.5
5.6	2.2
7.0	1.6
12.3	1.9
16.1	0.3
21.4	0.0
24.8	0.4
30.3	1.0
41.7	0.2
50.6	NA

Table S2: The deviations between the twice repeated measurements for different depths and field size d = 4 cm. NA = not available.

Depth [mm]	Deviation [%]
1	2.3
3.3	0.3
5.6	1.2
16.1	0.3
17.3	1.7
21.4	1.1
22.6	1.2
24.8	1.2
30.3	2.1
41.7	2.4
50.6	NA

Table S3: The deviations between the twice repeated measurements for different depths and field size d = 6 cm. NA = not available.

Depth [mm]	Deviation [%]
1	2.3
3.3	1.1
5.6	0.5
16.1	2.8
17.3	1.1
21.4	0.04
22.6	0.1
24.8	0.2
30.3	2.8
41.7	1.0
50.6	NA

Table S4: The deviations between the twice repeated measurements for different depths and field size d = 8 cm. NA = not available.

Depth [mm]	Deviation [%]
1	1.1
3.3	0.4
5.6	2.8
16.1	2.0
17.3	1.4
21.4	2.6
22.6	1.9
24.8	1.3
30.3	2.2
41.7	1.8
50.6	NA

Table S5: The deviations between the twice repeated measurements for different depths field size 10x10 cm. NA = not available.

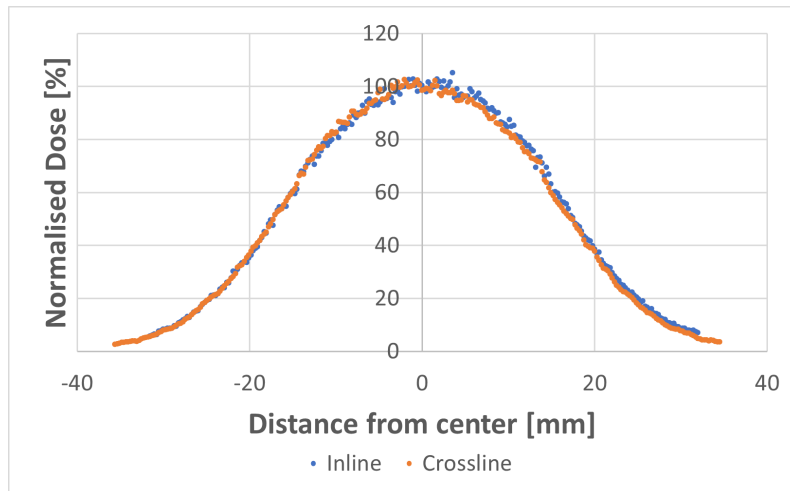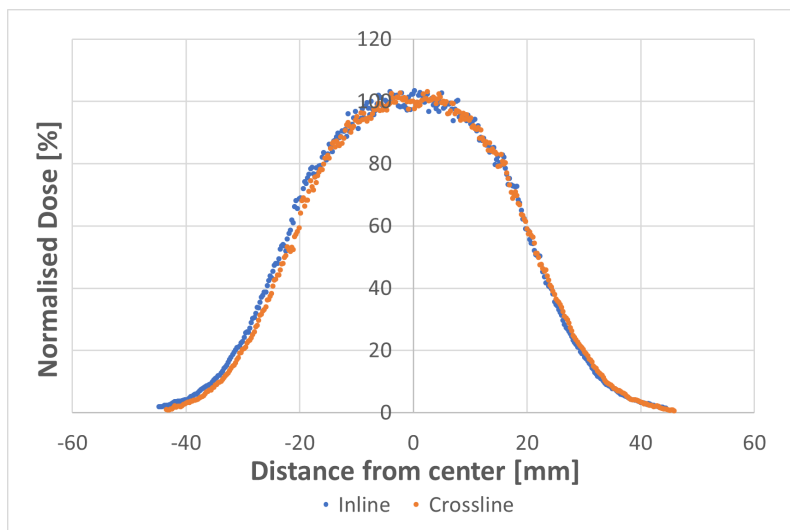| Depth [mm]	Deviation [%]
1	2.5
3.3	1.2
5.6	3.7
16.1	1.8
17.3	1.3
21.4	0.3
22.6	0.7
24.8	0.4
30.3	2.9
41.7	1.1
50.6	NA

Figure S12: Dose profile at 2 cm depth, in inline and crossline directions for a field with d = 3 cm.

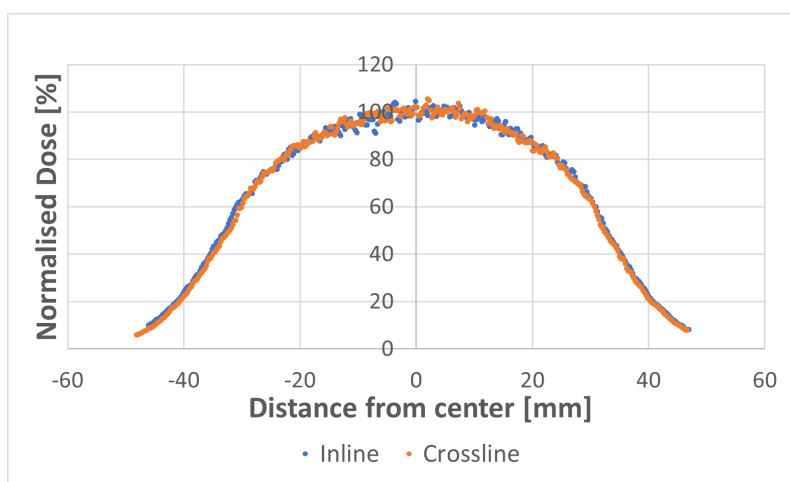Figure S13: Dose profile at 2 cm depth, in inline and crossline directions for a field with d = 4 cm.

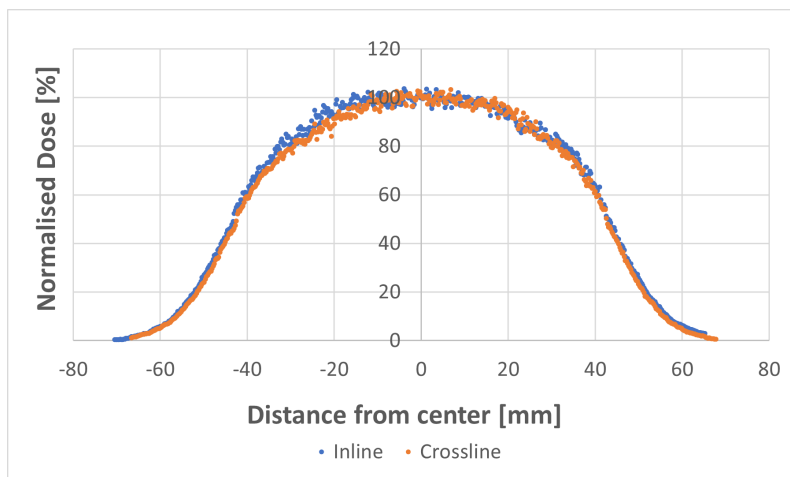Figure S14: Dose profile at 2 cm depth, in inline and crossline directions for a field with d = 6 cm.

Figure S15: Dose profile at 2 cm depth, in inline and crossline directions for a field with d = 8 cm.
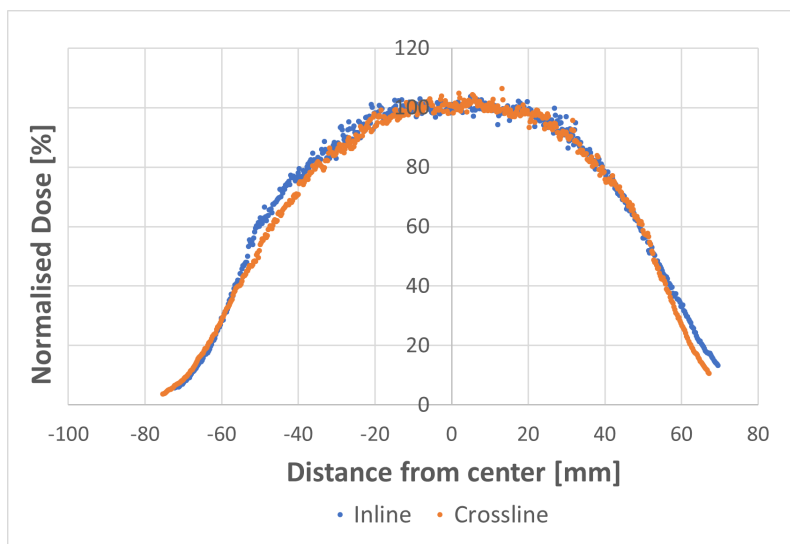

Figure S16: Dose profile at 2 cm depth, in inline and crossline directions for a field dimensions 10 x 10 cm.